Messinian carbonate-rich beds of the Tertiary Piedmont Basin (NW Italy): microbially-mediated products straddling the onset of the salinity crisis

Messinian carbonate-rich beds of the Tertiary Piedmont Basin (NW Italy): microbially-mediated products straddling the onset of the salinity crisis

Francesco Dela Pierre[1, 2*], Pierangelo Clari[1], Elisa Bernardi[1], Marcello Natalicchio[1], Emanuele Costa[1], Simona Cavagna[1], Francesca Lozar[1], Stefano Lugli[3], Vinicio Manzi[4,5], Marco Roveri[4,5], Donata Violanti[1,2]

1) Università di Torino, Dipartimento di Scienze della Terra, Via Valperga Caluso 35, 10125, Torino, Italy

2) CNR IGG , Sezione di Torino, Via Valperga Caluso 35, 10125, Torino, Italy

3) Università di Modena e Reggio Emilia, Dipartimento di Scienze della Terra, Piazza S. Eufemia 19, 41100, Modena, Italy

4) Università di Parma, Dipartimento di Scienze della Terra, Via G.P. Usberti 157/A, 43100, Parma, Italy

5) Alpine Laboratory of Palaeomagnetism (ALP), Via Madonna dei Boschi 76, 12016, Peveragno (CN), Italy

* Corresponding author

E-mail address: francesco.delapierre@unito.it

Phone: +39 0116705198

Fax: +39 0116705339

ABSTRACT

The seven Messinian microbial carbonate-rich layers cropping out in the Pollenzo section (Tertiary Piedmont Basin, NW Italy) are interbedded with a precession-related cyclic succession composed of euxinic shale/marl couplets and straddle the onset of the Messinian salinity crisis (MSC). A sharp change of sedimentological, compositional and geochemical characteristics was observed from the onset of the MSC onward, suggesting strong differences in the mechanisms responsible for carbonate precipitation. Pre-MSC beds are mainly composed of dolomite and are interpreted as the product of early diagenesis, formed by bacterial sulphate reduction in the shallow subsurface along the sulphate-methane interface. Dolomite precipitation was temporarily enhanced by an upward flux of methane-rich fluids, possibly sourced by gas hydrate destabilisation. Conversely, from the onset of the MSC onward, carbonate beds are thinly laminated and show abundant filaments interpreted as *Beggiatoa*-like bacteria, while calcite (and aragonite) are the dominant authigenic phases. These beds are interpreted as microbialites, resulting from the lithification of chemotrophic bacterial mats dominated by sulphide-oxidizing bacteria. The carbonate necessary for their preservation was provided by bacterial sulphate reduction. These microbialites, that appear as the deeper water counterpart of bottom-grown selenite layers deposited in the marginal part of the basin, formed on an anoxic sea bottom under a density stratified water column. The high sulphate concentration in the pore waters, related to the presence of concentrated brines and to the regeneration of sulphate by sulphide-oxidizing bacteria, is considered as the driving factor controlling the mineralogical change from dolomite to calcite and aragonite. Finally, the sharp shift toward negative $\delta^{18}O$ values of carbonates, observed from the onset of the MSC onward, was probably related to fractionation processes operated by sulphate-reducing bacterial communities in the pore waters. This suggests that care must be taken, when dealing with microbial carbonates, in the interpretation of the oxygen isotope values in term of fluctuating salinity condition of the water mass. In conclusion, this study suggests that the onset of the MSC had a strong impact on microbial populations governing

carbonate precipitation, in a sector of the basin dominated by depositional conditions not suitable for gypsum precipitation.

Key words: bacterial sulphate reduction, bacterial sulphide oxidation, Messinian salinity crisis, microbial mats, Tertiary Piedmont Basin.

1. Introduction

Studies of modern environments and culture experiments have shown that microbially-induced carbonate precipitation is a common process active in various types of marine sediments (*e.g.* Irwin et al., 1977; Vasconcelos et al., 1995; Wright and Oren, 2005). In particular, sulphate-reducing bacteria are considered to play a fundamental role in triggering the precipitation of different carbonate minerals (calcite, aragonite, dolomite) in a wide range of organic-rich sediments from peritidal microbial mats (*e.g.* Baumgartner et al., 2006, Dupraz et al., 2009) to anoxic deep sea sediments (*e.g.* Meister et al. 2008). A prolonged and intense activity of the degradation of organic matter by sulphate-reducing bacteria can lead to the formation of lithified layers and masses, commonly referred to as microbialites. However, other prokaryotes are also thought to be related to carbonate precipitation and sediment lithification, including methanogenic archaea, anaerobic methane oxidizing communities, and cyanobacteria (see Wright and Oren 2005 and references therein). The correct identification of the prokaryotes involved in the formation of diagenetic carbonate bodies can provide fundamental information on the environmental conditions governing carbonate precipitation both at the sea bottom and in the shallow subsurface.

Microbial carbonate rocks are a common component of the Messinian salinity crisis (MSC) stratigraphic record. They have been mainly reported from: 1) the Terminal Carbonate Complex (Esteban, 1979), a syn- to post-evaporitic unit found in the western Mediterranean basins (*e.g.* Riding et al., 1998; Braga et al., 2006; Roveri et al., 2009) that is mostly composed of large

75 thrombolite and stromatolite domes (Feldmann and Mc Kenzie, 1997; Arenas and Pomar, 2010); 2)
76 the Calcare di Base, a composite unit found in Sicily and Calabria below the gypsum or passing
77 laterally into it (Decima et al., 1988; Garcia-Veigas et al., 1995; Oliveri et al., 2010). As
78 summarised by Manzi et al. (2011), the Calcare di Base was interpreted as a chemical precipitate
79 from concentrated brines immediately prior to evaporite deposition (Schreiber and Friedman, 1976;
80 Decima et al., 1988) and/or as a microbial product formed in a restricted basin (Bellanca et al.,
81 2001; Blanc-Valleron et. al., 2002). In particular, beds of carbonate "stromatolites" were reported
82 (Oliveri et al., 2010) and interpreted as the record of progressively shallower, more restricted and
83 hypersaline conditions, favouring the development of microbial communities at the sea floor
84 immediately prior to the onset of gypsum deposition (*e.g.* Rouchy and Caruso, 2006). Wide salinity
85 fluctuations and sharp dilution events of the brines have also been highlighted (Guido et al., 2007).
86 A complex diagenetic evolution, including microbial sulphate reduction coupled to the oxidation of
87 biogenic methane, was also proposed (Ziegenbalg et al., 2010, 2012). Similar beds were described
88 below the gypsum from other Mediterranean localities such as the Vena del Gesso basin (Vai and
89 Ricci Lucchi, 1977; Manzi et al., 2011) and Cyprus, where these features have been referred to as
90 stromatolites and considered to record basin shallowing and restriction (Rouchy and Monty, 1981;
91 Krijgsman et al., 2002; Orszag-Sperber et al., 2009).
92 A recent revisitation of the Calcare di Base in Sicily, Calabria and northern Apennines
93 (Manzi et al., 2011) showed that this unit actually consists of several types of carbonates formed in
94 different setting and during different stages of the Messinian salinity crisis. In particular, the unit
95 includes three types of carbonates: a) thin dolostone beds interbedded to tripolaceous facies,
96 representing the deep water equivalent of primary gypsum deposited in marginal basins during the
97 first MSC step (type 2); b) clastic bodies deposited during the second MSC stage (type 3); c) late
98 diagenetic products after original resedimented gypsum layers (type 1).
99 Thin carbonate beds are also known from the Piedmont succession, just below the gypsum
100 (Sturani, 1973). In previous studies (Sturani, 1976) these beds, that abruptly overlie lower

Messinian deep water marls, were interpreted as the record of a dramatic sea level fall (of the order of 200-500 m) at the onset of the MSC. This interpretation was based on the presence of a variety of features thought to indicate deposition in very shallow waters and subaerial exposure (stromatolitic lamination, desiccation and expansion cracks, calcite pseudomorphs after gypsum crystals). However, a recent revisitation of the MSC record of the southern margin of the Piedmont Basin (Dela Pierre et al., 2011) suggested that these carbonate beds actually straddle the onset of the MSC and that part of them are the lateral deep-water counterpart of the lowermost gypsum layers deposited in the shallow marginal part of the basin, hence corresponding to the type 2 Calcare di Base (*sensu* Manzi et al., 2011, see above) of the Sicilian succession.

In this paper we present the results of an integrated sedimentological, petrographical and geochemical study of Messinian carbonate beds, from the Pollenzo section. The results offer the opportunity to discuss the impact that the environmental changes related to the onset of the MSC had on microbial populations governing carbonate precipitation, in a sector of the basin dominated by depositional conditions not suitable for gypsum precipitation.

2. The Messinian salinity crisis

The MSC affected the Mediterranean basin between 5.96 and 5.33 Ma and resulted in the deposition of huge volumes of evaporites that are presently preserved both at the basin margins and in deep basinal areas, where they are buried below the abyssal plains of the Western and Eastern Mediterranean sea (*e.g.* Rouchy and Caruso, 2006). After the formulation of the desiccated deep basin model (Hsü et al., 1973; Cita et al., 1978), the nature and timing of the MSC events still remain the object of a lively scientific debate, mainly because a detailed correlation between the marginal sub-basins, that provide most of the outcropping successions (*e.g.* Clauzon et al., 1996; Krijgsman et al., 1999; Rouchy and Caruso, 2006; Manzi et al., 2007; Roveri et al., 2008; Lugli et al., 2010) and the deep basins, whose buried sedimentary record was analysed by seismic profiles,

127 is still lacking (Ryan, 1976; Bertoni and Cartwright, 2007; Lofi et al., 2011). Recently, a MSC
128 evolutionary model has been proposed (CIESM, 2008). This model derives from the two step
129 scenario of Clauzon et al. (1996) and envisages three MSC stages. During the first one (5.96-5.60
130 Ma) primary evaporites were deposited only in shallow, silled, peripheral basins (Primary Lower
131 Gypsum unit; Roveri et al., 2008). Carbonate microbialites are often reported below these deposits
132 (*e.g.* Rouchy and Monty, 1981; Rouchy and Caruso, 2006). Conversely, in deep basinal setting,
133 only euxinic shales and dolomite-rich beds (the type 2 Calcare di Base of Manzi et al., 2011) were
134 deposited during this stage. The absence of gypsum and the concomitant formation of dolomite
135 seem related to anoxic conditions, responsible for the decrease of the dissolved sulphate content via
136 organic matter degradation by bacterial sulphate reduction (De Lange and Krijgsman, 2010).
137 During the second MSC stage (5.60-5.55 Ma) the marginal basins underwent subaerial
138 exposure and erosion as evidenced by an erosional surface, referred to as the Messinian erosional
139 surface (Lofi et al., 2011). This surface can be traced basinward in a correlative conformity placed
140 at the base of thick accumulations of chaotic and resedimented evaporites, the Resedimented Lower
141 Gypsum unit (Roveri et al., 2008).
142 During the third stage (5.55-5.33 Ma) a rapid transition to environments characterised by
143 fluctuating salinity conditions is recorded by deposition of evaporites (Upper Evaporites) and clastic
144 sediments containing brackish to fresh water fossil assemblages. The reestablishment of fully
145 marine conditions at 5.33 Ma (Zanclean) marks the end of the salinity crisis.
146
147 **3. Geologic and stratigraphic setting**
148
149 The Tertiary Piedmont Basin (Figs. 1A, B) is filled with Upper Eocene to Messinian
150 sediments deposited unconformably on a wedge of Alpine, Ligurian and Adria basement units
151 juxtaposed in response to the collision between the Europe and Adria plates (*e.g.* Mosca et al.,
152 2009; Rossi et al., 2009). Messinian strata were deposited in a wide wedge top basin (Figs. 1B, 2A),

bounded to the north by the more external Apennine thrusts (Rossi et al., 2009; Dela Pierre et al., 2011). The shallow marginal zones are presently exposed in the northern (Torino Hill and Monferrato) and southern (Langhe) sectors of the Piedmont Basin, whereas the depocentral zones are buried below Pliocene and Quaternary sediments (Savigliano and Alessandria basins) (Fig.1A).

The succession begins with outer shelf to slope muddy sediments referred to as the Sant'Agata Fossili Marls (Tortonian-lower Messinian) that record progressively more restricted conditions heralding the onset of the MSC (Sturani and Sampò, 1973). This unit displays a precession-related cyclic stacking pattern, evidenced by the rhythmic repetition of euxinic shale/marl couplets (Lozar et al., 2010), and is followed at basin margin by the Primary Lower Gypsum unit (Fig. 2A). The latter shows the same precession-driven lithologic cyclicity, represented by shale/gypsum couplets (Dela Pierre et al., 2011). No *in situ* primary evaporites are documented in the depocentral zones, but seismic data show that their time equivalent sediments are represented by shales (Irace et al., 2010).

The transition between the shallow marginal area and the buried depocentre is exposed on the southern sector of the Piedmont Basin (Alba region) and was reconstructed in detail along a SW-NE transect (Dela Pierre et al., 2011) (Fig. 2B). On the basin margins, six Primary Lower Gypsum cycles were recognised, composed of bottom grown-selenite layers; the sixth bed represents a distinct marker bed referred to as the Sturani key-bed (Dela Pierre et al., 2011). Moving towards the NE (*i.e.* towards the depocentral zone), only two gypsum beds are present below this marker bed. In the Pollenzo section they overlie a cyclic succession of euxinic shales, marls and carbonate-rich beds (the object of this study), belonging from the lithostratigraphic point of view to the Sant'Agata Fossili Marls (Fig. 2B). Due to their position with respect to the Sturani key-bed, the uppermost three cycles must be considered as the deeper water equivalent of the lower cycles of the Primary Lower Gypsum unit deposited in marginal setting (Dela Pierre et al., 2011). This correlation is confirmed by bio-magnetostratigraphic data, indicating that the onset of the MSC

178 should be placed at Pollenzo three cycles below the first gypsum bed, in correspondence of the peak
179 abundance of the calcareous nannofossil *Sphenolithus abies* (Lozar et al., 2010).
180 The Primary Lower Gypsum unit is followed by resedimented and chaotic evaporites (Valle
181 Versa Chaotic Complex, Dela Pierre et al., 2007), that are considered to be equivalents of the
182 Resedimented Lower Gypsum unit (Fig. 2B) deposited during the second MSC stage (5.60-5.55
183 Ma). This latter unit is finally followed by fluvio-deltaic and lacustrine deposits (Cassano Spinola
184 Conglomerates) recording the third MSC stage (5.55-5.33 Ma), in turn overlain by Zanclean marine
185 clays (Argille Azzurre Formation).
186
187 *3.1 The Pollenzo section*
188
189 In this section, located along the Tanaro River, a complete Messinian succession,
190 comprising the Sant'Agata Fossili Marls, the Primary Lower Gypsum, the Resedimented Lower
191 Gypsum units and the Cassano Spinola Conglomerates, is exposed (Fig. 3). Only the Sant'Agata
192 Fossili Marls, in which the studied carbonate beds are hosted, will be described below. For the
193 chrono-biostratigraphic data of this unit and for the description of the overlying succession, the
194 reader is referred to Lozar et al. (2010) and Dela Pierre et al. (2011).
195 The Sant'Agata Fossili Marls consist of muddy marine sediments characterised by a
196 distinctive precession-driven cyclicity, given by the alternation of euxinic shale/marl couplets,
197 forming up to 3 m-thick cycles (Dela Pierre et al., 2011). A 80 m-thick slumped interval divides the
198 section into two portions (Fig. 3). The lower portion, below the slump, consists of seven cycles; in
199 the upper portion, above the slump, the lithologic cyclicity is enhanced by the regular repetition of
200 carbonate-rich beds easily distinguishable for their whitish colour (Fig. 4). Seven cycles (Pm1-Pm7)
201 with an average thickness of 3 metres were recognised, each one including a distinct carbonate bed.
202 The integration of physical-stratigraphic (position with respect to the Sturani key-bed) and
203 biostratigraphic data (peak abundance of the calcareous nannofossil *S. abies*), demonstrated that the

204 onset of the MSC must be placed at the base of cycle Pm5 (Lozar et al., 2010; Dela Pierre et al.
205 2011). Hence four pre-MSC cycles (Pm1-Pm4) are present, followed by three MSC cycles (Pm5-
206 Pm7) that correspond to the lowermost Primary Lower Gypsum cycles recognised in the marginal
207 part of the basin (Fig. 3).
208 Each pre-MSC cycles is composed of a basal layer of laminated euxinic shale, transitionally
209 followed by a calcareous marly bed that hosts a dm-thick carbonate-rich bed. The strong
210 impoverishment of foraminiferal assemblages, that include only rare stress tolerant planktic
211 (*Turborotalita quinqueloba* and *T. multiloba*) and benthic taxa (*Bolivina dentellata* and *Bulimina*
212 *echinata*), suggests the establishment of restricted conditions, a severe stratification of the water
213 column and the impoverishment in dissolved oxygen of bottom waters (Lozar et al., 2010). The
214 MSC cycles show analogous lithologic characteristics, but no marls were observed in cycle Pm6;
215 moreover the carbonate beds here show a laminated structure, not observed in the underlying ones
216 (see below). An hemi-ellipsoidal convex-upward indurated body has been observed 50 cm above
217 layer *e*, within cycle Pm6 (Fig.3).This feature was not reported in Dela Pierre et al. (2011) because
218 completely submerged at that time by the Tanaro River. Foraminifers and calcareous nannofossils
219 are extremely rare and disappear at the top of cycle Pm6, confirming the final disruption of the
220 water column and the definitive establishment of anoxic bottom conditions. The upper carbonate
221 bed (*g*, Figs. 3, 4) is overlain by the first gypsum-bearing cycle (Pg1, Fig. 3), that is composed of
222 laminated muddy siltstones followed by a 1-m thick massive selenite bed; this cycle corresponds to
223 the 4th cycle of the Primary Lower Gypsum unit (Dela Pierre et al., 2011).
224
225 **4. Methods**
226
227 Field studies of the lithology and geometry of the carbonate beds, including the relationships
228 with the host sediments, were carried out on the upper portion of the Sant'Agata Fossili Marls,
229 above the slump. Both the carbonate beds and the unconsolidated host sediments were sampled for

petrographic and geochemical analyses. Twelve standard thin sections of the most representative samples were studied under the optical microscope and were further analysed for their fluorescence, using a Nikon microscope equipped with a B-2a filter block (illumination source with an excitation wave length of 450-490 nm) (Department of Plant Biology, Torino University). Scanning Electron Microscopy (SEM) analyses were performed on 30 slightly etched polished surfaces using a SEM Cambridge Instruments Stereoscan 360 equipped with an energy-dispersive EDS Oxford Instruments Link System microprobe (Department of Earth Sciences, Torino University). Semiquantitative analyses on the amount of the carbonate fraction and on its mineralogical composition (calcite and dolomite) were carried out on 40 samples (including both the carbonate-rich beds and the host sediments) at the Inductively Coupled Plasma-Optical Emission Spectroscopy (ICP-OES) laboratory (Department of Earth Sciences, Torino University), using an IRIS II Advantage/1000 (Thermo-Jarrel Ash Corp.). As a first step, 2000 mg of sample powder were stirred for 48 h in 200 ml of distilled water, in order to dissolve the (diagenetic) gypsum possibly present in the sediments. The filtered solution was analysed and the amount of sulphur was measured. Assuming that all the sulphur derived from dissolution of gypsum (pyrite or silicates are not dissolved in distilled water), a corresponding stoichiometric amount of Ca^{2+} was then subtracted from to the whole Ca^{2+} pool (obtained in the further step) in order to avoid an overestimation of the carbonates. As a second step, 200 mg of sample powder were processed in 10 ml of hot acetic acid for 12 h, in order to dissolve the carbonates but at the same time preserving the silicates. The filtered solution was analysed and the amount of Ca^{2+} and Mg^{2+} was measured. The relative abundance of calcite and dolomite in the samples was calculated (after subtraction of the amount of Ca^{2+} derived from gypsum, as mentioned above) assigning the total amount of Mg^{2+}, with the corresponding amount of Ca^{2+}, to stoichiometric dolomite; the remaining Ca^{2+} was assumed to derive from calcite and was used to calculate the abundance of stoichiometric calcite. EDS analyses performed on some samples confirmed the near stoichiometric composition of calcite (less than 1%

255 of Mg^{2+}), and dolomite (51- 53 $CaCO_3$ mole%). The results of Inductively Coupled Plasma (ICP)
256 analyses (Table 1) are expressed as mass percent on the whole sediment.
257 Bulk rock C and O stable isotope analyses were performed on 22 samples from both
258 carbonate-rich beds and unlithified sediments at the ISO4 laboratory (Torino, Italy) and in the
259 *MARUM* Stable Isotope Laboratory (Bremen, Germany). The carbonate fraction was analysed
260 following the classical method (McCrea, 1950). The $^{13}C/^{12}C$ and $^{18}O/^{16}O$ ratios of the CO_2 were
261 obtained using Finnigan MAT 251 and 252 mass spectrometers. For the carbonate-rich beds, both
262 calcite and dolomite were measured, whereas in the unconsolidated sediments only calcite was
263 analysed. The isotopic ratios are expressed as $\delta^{13}C$ and $\delta^{18}O$ per mil versus the PDB standard (Fig.
264 3, Table 3); the analytical error is ±0.5‰ and ±0.1‰ for $\delta^{13}C$ and $\delta^{18}O$, respectively.
265
266 **5. Results**
267 *5.1. Lithology*
268
269 *5.1.1 Unconsolidated sediments*
270 In the host sediments, the carbonate content ranges from 10 to 41% and consists of both
271 calcite and dolomite that are mixed in variable proportions (Table 1). The total carbonate ranges
272 from 23 to 41% in the homogeneous marl and reaches the lowest values (<23%) in the laminated
273 shale. As a general rule, pre-MSC sediments contain a higher calcite fraction, probably related to
274 the higher content of skeletal grains (foraminifers and calcareous nannofossils), that are generally
275 very rare or even absent in MSC sediments.
276
277 *5.1.2 Pre-MSC carbonate-rich beds*
278 Pre-MSC beds (*a, b, c, d*) are dm- thick and are interbedded within the marly part of the
279 lithologic cycles (Pm1 to Pm4, Fig. 3). The lower and upper contacts are transitional, except for bed
280 *a* in which they are sharp (Fig. 5A). These beds are the product of local cementation of host

281 sediments and contain variable amounts of a silt-sized terrigenous fraction, mainly consisting of
282 mica flakes. All beds are strongly bioturbated (Figs. 5B, C), suggesting deposition on an
283 oxygenated sea bottom, and contain planktic and benthic foraminifers, and calcareous nannofossils.
284 The intergranular cement mostly consists of idiomorphic rhombohedral crystals of
285 dolomite, ranging in size from 2 to 10 μm (Fig. 5D). Calcite is also present, both of biogenic and
286 diagenetic origin. The mixture is confirmed by data from ICP analyses (Tables 1 and 2); they show
287 that in beds *a*, *b* and *d* dolomite represents 91.9, 68.0 and 83.3% of the total carbonate content
288 (76.1, 63.1 and 45.1% respectively over the bulk composition). Conversely in bed *c* the total
289 carbonate fraction (48.2%) consists of similar proportions of calcite and dolomite (51.7 and 48.3%,
290 respectively) (Fig. 3, Table 2). Pyrite framboids, up to 10 mμ across, are very common in all beds
291 (Fig. 5E).
292
293 *5.1.3 MSC carbonate-rich beds*
294 Beds deposited during the salinity crisis are about 20 cm-thick and show transitional
295 contacts with the host sediments (Fig. 6A). Bed *e* is located at the top of the marly interval and
296 contains mm-sized intraclasts, floating in a clotted micrite matrix containing rare foraminifers. A
297 remarkable feature is the presence of contractional cracks developed around the clasts
298 (circumgranular cracks) (Fig. 6B). Beds *f* and *g* show different features, because they are not
299 bioturbated and display a well-developed lamination. Bed *f* lies in strongly laminated shales (no
300 marl was observed in cycle Pm6) and shows a lamination marked by the alternation of mm-thick
301 whitish and grey wrinkled laminae (Fig. 6C). The formers are composed of clotted micrite, contain
302 abundant pyrite framboids and are crossed by a network of mm-wide contractional cracks, running
303 perpendicular to the lamina surfaces, that are empty or filled with late diagenetic gypsum (Fig. 6D).
304 These laminae contain abundant fish vertebrae and scales. The grey laminae are richer in
305 terrigenous material, mostly represented by clay particles and mica flakes (Fig. 6D). At the
306 boundary between the two types of laminae, cracks were commonly observed. Micrite laminae

307 exhibit a stronger epifluorescence than the terrigenous ones, suggesting a higher content in organic
308 matter (Fig. 6E). Moreover, epifluorescence microscopy permits the recognition of filaments, up to
309 100 μm across and more than 300 μm long, showing different fluorescence shades (Fig. 6E). Bed *g*
310 is similar to bed *f*, except it is made up of more wrinkled and thinner laminae (less than 1 mm).
311 Pyrite framboids are abundant and are frequently grouped together to mimic filaments about 100
312 μm across and up to 800 μm long (Figs. 7A, C). Epifluorescence observations reveal that filaments
313 show a stronger fluorescence than the enclosing matrix (Fig. 7D). The same features, despite less
314 abundant, were observed in bed *f*.
315 Unlike the pre-MSC beds, the carbonate fraction of the salinity crisis layers is dominated by
316 calcite whereas dolomite is subordinate; frequently micron-sized calcite crystals show a globular
317 shape with a central hollow, suggesting a possible microbial origin (Cavagna et al., 1999). This type
318 of crystals (Fig. 7B) was observed also within the filaments, together with abundant pyrite
319 framboids. Remarkably, no terrigenous grains, abundant in the enclosing matrix, were observed
320 within the filaments. The predominance of calcite over dolomite is confirmed by ICP analyses; in
321 beds *e*, *f* and *g* calcite is 80.2, 84.1 and 94.8% of the total carbonate content (84.6, 69.1 and 59.0%,
322 respectively) (Fig.3, Table 2).
323
324 *5.1.4 The hemi-ellipsoidal body*
325 The hemi-ellipsoidal cemented body observed within cycle Pm6 is 1.70 metres by 1 metre in
326 size and shows transitional lateral contacts with the host laminated shale (Fig. 8A). Its most
327 remarkable feature is the wrinkled lamination (Fig. 8B), given by the alternation of submillimetric
328 whitish and grey lamine, that strongly resembles the structure described as the “stromatolites” of the
329 Sicilian Calcare di Base (Oliveri et al., 2010). The whitish laminae are composed of filaments, 150
330 μm across and up to few millimetres long (Fig. 8C), that are irregularly oriented or with their
331 maximum dimension parallel to the lamina surface. The filaments are made of clotted micrite,
332 composed of micron-sized strongly epifluorescent calcite crystals (Figs. 8D, F). They are

commonly curved and are surrounded by fringing aragonite (Figs. 8E, F). No terrigenous grains were observed in the filaments, as in beds *f* and *g*. Grey laminae are richer in terrigenous grains, are laterally discontinuous and seal the undulating microtopography formed by the former white laminar structures. Moreover, mm-sized *fenestrae*, likely resulting from dissolution of former gypsum crystals, are present. Pyrite framboids, up to 20 μm across, are very common in both types of laminae and frequently cap acicular aragonite crystals (Fig. 9).

5.2. Stable isotope data

5.2.1 Unconsolidated sediments

In both pre-MSC and MSC cycles, the $\delta^{13}C$ values are around zero (Fig. 3, Table 3), suggesting carbonate precipitation from a fluid in isotopic equilibrium with sea water. The weak ^{13}C depletion observed in some samples from cycles Pm1 ($\delta^{13}C = –6.5‰$), Pm6 ($\delta^{13}C = –5‰$) and Pm7 ($\delta^{13}C = –4.7‰$) points to the contribution of diagenetic carbon from decaying organic matter. All samples are characterised by low $\delta^{18}O$ values, with a general trend towards more negative values in the MSC sediments (cycle Pm5-Pm7). The interpretation of these negative $\delta^{18}O$ values is not straightforward, because the analysed carbonate fraction is sparse (<23%) and the resultant values can reflect the contribution of different carbonate pools (detrital, skeletal, diagenetic), mixed in unknown ratios. However, these low values, commonly interpreted as the result of an overall "freshening" of the water mass under the increased influx of fresh water (*e.g.* Blanc-Valleron et al., 2002), may reflect complex microbial fractionation processes on the oxygen pool (see paragraph 6.2.2).

5.2.2 Pre-MSC carbonate-rich beds

A significant ^{13}C depletion was observed for both dolomite and calcite in beds *a* and *b* ($\delta^{13}C_{dol}$ = –19.8 and –21‰; $\delta^{13}C_{ca\,l}$ = –16.7 and –14.5‰, respectively). In the upper two pre-MSC beds (*c* and *d*) less negative values were instead measured for both minerals (–4.4 and –5.2‰ for dolomite; –9.2 and –5.7‰ for calcite, respectively). Positive $\delta^{18}O_{dol}$ values were observed in all pre-MSC beds (Fig. 3, Table 3): the stronger ^{18}O enrichment was measured in beds *a* ($\delta^{18}O_{dol}$ = +7‰) and *b* ($\delta^{18}O_{dol}$ = + 6.9‰), whereas in beds *c* and *d* lower values were found ($\delta^{18}O_{do\,l}$ = +1.3 and +3.6‰, respectively). More negative values were observed for calcite. In beds *a* and *b* the $\delta^{18}O_{cal}$ is +5.7 and –1.0‰, respectively, whereas in beds *c* and *d* it is –3.9 and –1.5‰ (Fig. 3, Table 3).

5.2.3 MSC carbonate-rich beds

In the salinity crisis beds, the $\delta^{13}C$ values of both dolomite and calcite are moderately negative (from –5 to –3.9‰ for dolomite and from –7.9 to –6.7‰ for calcite). A stronger ^{13}C depletion was measured for the calcite of the hemi-ellipsoidal body (cycle Pm6), with values around –8.5‰. For what concerns the $\delta^{18}O$, a remarkable shift towards negative values was observed. The $\delta^{18}O_{dol}$ values range from –6.1 to –4.9‰ whereas the $\delta^{18}O_{cal}$ are more negative (from –6.5 to –8.8‰). The hemiellipsoidal body yelded $\delta^{18}O_{cal}$ values as low as –7.7‰.

6. Discussion

6.1. Pre-MSC beds: early diagenetic products from the shallow subsurface

In pre-MSC beds, the authigenic carbonate fraction is dominated by dolomite, mixed with variable amounts of calcite whose specific origin (detrital, skeletal and/or diagenetic) could not be

382 determined. The beds formed in strongly bioturbated sediments, deposited on an oxygenated sea
383 bottom. The absence of traces of exposure of the indurated sediments at sea floor *(e.g.* firm ground
384 burrows, borings) suggests that carbonate precipitation occurred within the sedimentary column. On
385 the other hand the high authigenic carbonate content (45-76%) indicates that these beds formed in
386 the shallow subsurface, within still porous mud not yet affected by mechanical compaction.
387 Studies of modern environments and culture experiments have shown that dolomite
388 precipitation in the subsurface is induced by the metabolic activity of sulphate-reducing bacteria
389 that, by degrading organic matter, consume sulphate ions and increase overall alkalinity thus
390 overcoming the kinetic inhibition to dolomite precipitation (*e.g.* Baker and Kastner, 1981; Compton
391 et al., 1988; Vasconcelos et al., 1995; Wright and Oren, 2005; Baumgartner et al., 2006; Meister et
392 al., 2007; Wacey et al., 2008). In modern deep sea organic-carbon-rich hemipelagic sediments,
393 bacterial sulphate reduction is controlled by the downward diffusion of sulphate from sea water
394 (Compton, 1988; Wright and Oren, 2005). In these conditions, dolomite can precipitate from anoxic
395 sulphate-free pore waters, at the lower boundary of the sulphate-reducing zone. In present-day open
396 marine environments the depth of this surface, that corresponds to the sulphate-methane interface,
397 ranges from few metres up to few tens of metres, depending on the porosity and on the content and
398 type of organic matter (*e.g.* Borowski et al., 1999; Fossing et al., 2000; D'Hondt et al., 2002; Treude
399 et al., 2005; Jørgensen and Kasten, 2006). Apart from carbonate, sulphate reduction provides
400 hydrogen sulphide that subsequently can react with iron to form sulphide minerals (*e.g.* pyrite).
401 Carbonate precipitation at the sulphate-methane interface is however quantitatively limited and
402 commonly goes unnoticed in most sedimentary sequences (*e.g.* Raiswell and Fisher, 2004). In two
403 cases it becomes significant and may give origin to well recognizable carbonate-cemented layers: 1)
404 if large amounts of upward rising methane-rich fluids reach this geochemical interface; in this case
405 abundant carbonate (calcite, aragonite and dolomite) can precipitate resulting in extensive
406 cementation of the flushed sediments (*e.g.* Irwin et al., 1977; Raiswell, 1987; Raiswell and Fischer,
407 2000; Campbell, 2006; Ussler and Paull, 2008). Carbonate precipitation is induced by a consortium

of sulphate-reducing bacteria and methanotrophic archaea (Boetius et al., 2000), responsible for the anaerobic oxidation of methane; 2) if the sulphate-methane interface remains stationary within the sedimentary column for a prolonged time interval, resulting in focused dolomite precipitation; in this case, a distinct dolomite-rich bed can form even though the supply of methane-rich fluids from below is negligible (Meister et al., 2007, 2008).

The bed-parallel geometry of the Pollenzo pre-MSC beds suggests that dolomite precipitation occurred at a geochemical interface parallel to the sea bottom. In this regards the co-occurrence of authigenic carbonate and pyrite and isotopic data suggests that these beds may have formed at the sulphate-methane interface. In particular, the (moderately) negative $\delta^{13}C$ values measured in diagenetic dolomite of the lower two beds (*a* and *b*) ($\delta^{13}C$ around –20‰), points to the contribution of anaerobic oxidation of methane in dolomite precipitation (Fig. 10A). The moderate ^{13}C depletion (compared to typical methane-derived carbonates in which $\delta^{13}C$ values as low as –60‰ are commonly measured; *e.g.* Peckmann and Thiel, 2004) may reflect the mixture of methane-derived carbon with other sources, such as heavier hydrocarbons (Roberts and Aharon, 1994), marine dissolved inorganic carbon or skeletal material of marine organisms, that are actually present in these beds (*e.g.* Peckmann and Thiel, 2004; Natalicchio et al., 2012). The same mechanism can explain the $\delta^{13}C$ signature of calcite.

Conversely, the less negative $\delta^{13}C$ values of beds *c* and *d* ($\delta^{13}C$ around –5‰) suggest that dolomite precipitation was induced by organoclastic bacterial sulphate reduction alone, as the upward methane flux ceased completely (Fig. 10B). These indurated layers likely developed along a temporarily fixed sulphate-methane interface that favoured focused dolomite precipitation. Sulphate reduction alone, however, was able to produce only a lesser amount of authigenic dolomite with respect to anaerobic oxidation of methane, as indicated by geochemical data and by the minor induration of these beds.

The oxygen isotope record of dolomite (the predominant carbonate mineral) reveals that beds *a* and *b* are significantly enriched in the heavy ^{18}O isotope (Fig. 3, Table 3). Three mechanisms can explain such an enrichment:

a) evaporation of sea water (McKenzie et al., 1979). This mechanism, commonly invoked to explain the ^{18}O enrichment of Messinian carbonates (*e.g.* Rouchy et al., 1998; Bellanca et al., 2001; Blanc-Valleron et al., 2002) should in our case be ruled out, because these beds formed before the onset of the MSC. Moreover, it strongly contrasts with the negative values of host sediments;

b) upward movement of deep fluids whose isotopic composition was modified by dehydration of smectite clay minerals (*e.g.* Dählmann and De Lange, 2003). The possible role played by this process can not be ruled out because of the lack of information on the source fluids and on clay mineralogy of underlying sediments;

c) flushing of sediments by methane-rich fluids sourced by gas hydrate destabilisation. This mechanism is consistent with the association of positive $\delta^{18}O$ values with negative $\delta^{13}C$ ones, as already suggested for lower Messinian dolomite layers and concretions found in the eastern part of the Piedmont Basin (Dela Pierre et al., 2010; Martire et al., 2010; Natalicchio et al., 2012), Spain and Northern Morocco (Pierre and Rouchy, 2004). Conversely, the lower oxygen values measured in beds *c* and *d*, that are coupled with slightly negative $\delta^{13}C$ ones, suggest that the input of ^{18}O-enriched fluids, ceased together with the demise of methane-rich fluids.

As already mentioned, the more negative $\delta^{18}O_{cal}$ values probably reflect the mixing of authigenic and sedimentary calcite. Positive values were only observed in bed *a*, in which the scarce calcite content (8.1%) is likely diagenetic and cogenetic with dolomite.

6.2. MSC beds

A sharp change of sedimentological, compositional and geochemical characteristics is observed in the MSC beds. This change is shown by the following features that will be discussed

458 separately below: a) the presence of wrinkled laminae containing filament remains, and of
459 contractional cracks; b) the sharp decrease of the dolomite content and the concomitant increase of
460 the calcite (and aragonite) content; c) the negative $\delta^{18}O$ values recorded both in calcite and
461 dolomite. The carbon isotope data are instead comparable to those of the underlying pre-MSC beds
462 and of the host sediments, testifying to the incorporation of light organic carbon in the authigenic
463 phase.
464
465 *6.2.1. Wrinkled laminae, filaments and contractional cracks: vestiges of chemotrophic microbial*
466 *mats?*
467 The submillimetric wrinkled lamination and the peloidal clotted microfabric of the micrite
468 laminae, observed in beds *f* and *g* and in the hemi-ellipsoidal body of cycle Pm6, are typical
469 features of carbonate microbialites, *i.e.* organo-sedimentary deposits formed by the activity of
470 benthic microbial communities (Dupraz and Visscher, 2005; Dupraz et al., 2009; Oliveri et al.,
471 2010). Compelling evidence of the involvement of microbial mats in the formation of laminated
472 structure is given by the remains of microbial filaments, well recognizable in epifluorescence (Fig
473 6E) that in beds *f* and *g* are underlined by a concentration of pyrite framboids (Figs.7C, D).
474 Microbial filaments have been first observed in Messinian gypsum crystals (the so called *spaghetti*-
475 like structures; Vai and Ricci Lucchi, 1977) and interpreted as remains of filamentous
476 photosynthetic cyanobacteria (*e.g. Scytonema*) on the basis of size and internal structure (Rouchy
477 and Monty, 1981; Panieri et al., 2010), thus providing evidence for shallow water (photic)
478 depositional conditions (but see also the discussion about the relevance of these features for water
479 depth determination in Lugli et al., 2010). Analogous features were then observed in carbonate
480 deposits below the gypsum and were considered either as faecal pellets (Guido et al., 2007) or as
481 cyanobacteria remains on the basis of their similarities with the *spaghetti* structures (Rouchy and
482 Monty, 1981; Orszag-Sperber et al., 2009). Hence, also these carbonates were classically

483 interpreted as shallow water deposits recording stressed environmental conditions heralding the
484 onset of the MSC.

485 The absence of terrigenous grains within the Pollenzo filaments allows to rule out their
486 faecal origin. An alternative hypothesis is that these filaments represent remains of colourless
487 sulphide-oxidizing bacteria like *Beggiatoa*, *Thioplaca* and *Thiotrix*. These giant bacteria, that can
488 reach a diameter of 750 μm and a length of several cm, obtain the energy necessary for their life
489 from the oxidation of sulphide by using oxygen or nitrate as electron acceptors (Schulz and
490 Jørgensen, 2001) and do not necessitate light as the driving energy source. In modern settings, they
491 form dense microbial mats (known as chemotrophic-dominated mats) thriving at different water
492 depth (from peritidal to bathyal settings), especially at sites where high concentration of sulphide is
493 available at the sea bottom (*e.g.* Bailey et al., 2009) such as hydrothermal vents (*e.g.* Jannasch et al.,
494 1989) and cold seeps (Larkin et al., 1994, Sahling et al., 2002; Teichert et al. 2005). However,
495 sulphide-oxidizing bacteria are also known to form extensive felt-like mats where organic-rich
496 sediments are exposed at the sea floor in contact with either oxic (Schulz et al., 1999) or oxygen-
497 depleted waters, such as the continental shelf off Peru (Gallardo, 1977; Fossing et al., 1995) or the
498 Danish Limfjorden (Mussmann et al. 2003). In these cases the bacteria use nitrate (and not oxygen)
499 as electron acceptor for oxidizing sulphide to sulphate.

500 Though there are substantial similarities between the filamentous cyanobacteria and the
501 sulphide-oxidizing bacteria and their distinction is difficult on morphology only, we propose that
502 the Pollenzo filaments are remains of sulphide-oxidizing bacteria on the basis of the following
503 elements: a) their diameter (>100 μm), that is close to that of living forms. On the contrary,
504 cyanobacteria filaments rarely exceed 80 μm (*e.g.* Schulz and Jørgensen, 2001); b) the curved shape
505 of some filaments (Fig. 8E) consistent with the chemotactic behaviour of these prokaryotes that
506 often change their direction in the search of optimal concentrations of oxygen or nitrate (*e.g.*
507 Møeller et al., 1985); c) the concentration of pyrite framboids outlining the filament shape (beds *f*
508 and *g*, Figs. 7C, D). Living sulphide-oxidizing bacteria host elemental sulphur globules within the

509 cytoplasm, that can be further preserved as sulphur-containing minerals associated to the
510 filamentous body fossil (*e.g.* Bailey et al., 2009); d) the lack of any remain of shallow water
511 macrobiota that should accompany photosynthetic mats. The only features that could suggest a
512 shallow water origin for these laminated layers are the contractional cracks, either developed around
513 clasts and nodules (circumgranular cracks, Fig. 6B) or placed parallel and perpendicular to the
514 bedding (Fig. 6D). Similar features were previously interpreted as desiccation structures and hence
515 considered as a compelling evidence of the subaerial exposure of the Piedmont basin at the onset of
516 the MSC (Sturani, 1973). However, the geometry of crack, that are developed especially across the
517 carbonate-rich laminae and thin out both in the under- and overlying terrigenous laminae, contrasts
518 with an origin by subaerial exposure and desiccation. The microbial origin for the carbonates may
519 provide an alternative explanation for the genesis of these cracks, that can be interpreted as the
520 product of syneresis, related to the decay of bacterial extracellular polysaccharide substances (EPS)
521 binding clay particles (*e.g.* Dewhrust et al., 1999; Hendry et al., 2006) in a subaqueous
522 environment.

523 On this basis, beds *f* and *g* and the hemi-ellipsoidal body of cycle Pm6 are interpreted as the
524 product of the lithification of chemotrophic microbial mats dominated by sulphide-oxidizing
525 bacteria. Unlike their photosynthetic counterpart, chemotrophic mats are rarely preserved in the
526 fossil record, because the metabolism of sulphide-oxidizing bacteria increases acidity and
527 consequently induces carbonate dissolution rather than precipitation (*e.g.* Petrash et al. 2012). Their
528 preservation can however take place if other biogeochemical processes trigger the rapid
529 precipitation of authigenic carbonates necessary for the entombment of the delicate filaments before
530 their complete decay. This may explain why putative fossil remains of sulphide-oxidizing bacteria
531 are chiefly reported from ancient seep carbonate deposits, where anaerobic oxidation of vigorous
532 methane fluxes induced extensive syndepositional carbonate precipitation (Peckmann et al., 2004).
533 Described examples of filaments attributed to the genus *Beggiatoa* have been reported from cold
534 seep deposits of the Miocene of Italy (Cavagna et al., 1999; Peckmann et al., 2004; Barbieri and

535 Cavalazzi, 2005) and the Oligocene of Poland (Bojanowski, 2007). Another example is the
536 Messinian Calcare di Base of Sicily in which *Beggiatoa* filaments are entombed in a clotted
537 peloidal dolomicrite resulting from bacterial sulphate reduction (Oliveri et al., 2010).
538 The slightly depleted $\delta^{13}C$ values of the Pollenzo beds exclude a significant contribution of
539 anaerobic oxidation of methane and suggest that the main process responsible for carbonate
540 precipitation was degradation of organic matter via bacterial sulphate reduction. The characteristics
541 of the MSC beds allow to envisage the following scenario (Figs. 11, 12): changed environmental
542 conditions (anoxia of bottom waters, see below) favoured the shift of sulphate-reducing bacteria
543 communities toward the sea bottom and their establishment immediately below it, where they could
544 rely on abundant "fresh" organic matter; bottom anoxia actually inhibited aerobic oxidation of the
545 organic remains reaching the sea bottom (Fig. 11). Along with carbonate precipitation, bacterial
546 sulphate reduction provided an upward flux of hydrogen sulphide that sustained sulphide-oxidizing
547 bacterial communities at the sea floor. Due to bottom anoxia, nitrate was used as electron acceptor
548 by these prokaryotes for oxidizing sulphides to sulphates (Fig.12A). Intervals of higher sediment
549 input and increase of continental runoff, recorded by the laminae richer in terrigenous grains,
550 resulted in the aggradation of the sea bottom (Fig.12B). In these renewed conditions, microbial
551 communities were forced to migrate upward and the sea bottom was covered by a "new" mat
552 dominated by sulphide oxidizers. The availability of abundant and "fresh" organic matter increased
553 the rate of sulphate reduction in the shallow subsurface, and resulted in the rapid precipitation of
554 large amounts of carbonates preserving the previously formed mat (Fig. 12C). The repetition of
555 these processes through time led to the formation of the laminated structure that characterizes these
556 rocks. According to the proposed scenario, sulphide oxidation, that promoted acidity and carbonate
557 dissolution, was hence spatially and temporally decoupled from the alkalinity generated by sulphate
558 reduction inducing carbonate precipitation. EPS degradation prior to complete lithification was
559 responsible for the opening of contractional cracks. These features are also observed in bed *e*,
560 confirming the active role played by microbial activity in its formation.

561 The hemi-ellipsoidal body within cycle Pm6 differs from under-and overlying beds for its
562 geometry and for the more varied authigenic carbonate composition, including aragonite. This
563 feature likely developed above a local source of decomposing organic matter, able to sustain an
564 intense activity of the same bacterial consortia described above, as observed today around whale
565 falls (*e.g*. Treude et al., 2009) or sunken woods (*e.g.* Palacios et al., 2009). Enhanced bacterial
566 activity was responsible for the formation of large amount of calcite, that was followed by
567 precipitation of the aragonite fringes rimming the bacterial filaments.
568
569 *6.2.2 The change from dolomite to Ca-carbonates and the oxygen isotope composition of MSC*
570 *beds*
571 The other points to be discussed are: a) the mineralogical change recorded from the MSC
572 onset onward, evidenced by the sharp increase in the calcite content and by the appearance of
573 aragonite in the hemi-ellipsoidal body; b) the negative $\delta^{18}O$ values of the MSC carbonates.
574 Although still discussed (Sánchez-Román et al., 2009), the concentration of sulphate in the
575 pore waters is a critical factor controlling the composition of bacterially-induced carbonate
576 minerals. In particular, if the concentration of sulphate is high, dolomite is inhibited and other
577 carbonates (aragonite, calcite, Mg-calcite,) do form (*e.g.* Baker and Kastner, 1981; Kastner, 1984;
578 Wright and Oren, 2005). At Pollenzo, the main factor driving carbonate precipitation both in pre-
579 MSC and in MSC layers was bacterial sulphate reduction. However in pre-MSC beds the sulphate
580 in pore waters was exclusively supplied by normal salinity sea water and carbonate precipitation
581 took place within the sedimentary column. Under these conditions, all sulphate was consumed by
582 bacterial sulphate reduction and dolomite precipitation took place from sulphate-free pore waters
583 along the sulphate-methane interface.
584 On the contrary, MSC beds and the hemi-ellipsoidal body formed at the sea bottom in
585 contact with sulphate-enriched bottom waters, being these layers the lateral equivalents of bottom-
586 grown selenite beds formed in the shallower part of the basin, some tens of kilometres apart.

587 Moreover, the sulphate pool was continuously replenished by sulphide oxidation in the
588 chemotrophic microbial mats. As a consequence, sulphate could not be totally consumed, even in
589 the presence of an intense bacterial sulphate reduction, and precipitation of Ca-carbonates (calcite,
590 aragonite) was favoured. Minor amounts of dolomite, occupying the residual pore space formed
591 only after sediment burial, when all sulphate was consumed. This last mechanism was also
592 responsible for the minor amount of dolomite in the host sediments.

593 The shift towards more negative $\delta^{18}O$ values observed in MSC carbonates ($-6.5 < \delta^{18}O_{cal} < -$
594 8.8‰ PDB; $-4.9 < \delta^{18}O_{dol} < -6.1$‰ PDB) compared to the underlying pre-MSC ones remains a still
595 unresolved question. Such ^{18}O depletion is reported from carbonates just below the first evaporitic
596 deposits in other Mediterranean basins (even if less severe than at Pollenzo) and is interpreted as the
597 result of sharp dilution events pointing to the isolation of the basin(s) prior to the onset of gypsum
598 deposition (*e.g.* Rouchy et al., 1998; Bellanca et al., 2001; Blanc-Valleron et al., 2002). This
599 interpretation is hardly reconcilable with the Pollenzo beds, that are the lateral equivalents of
600 gypsum. Alternative hypotheses have been proposed, that point to microbial sulphate consumption
601 as a possible source of ^{16}O enrichment in the microenvironments of carbonate precipitation (Sass et
602 al., 1991). The effects of this process on oxygen isotopic ratios both of sulphate and water have
603 been studied, since the seminal work of Lloyd (1968), with theoretical and experimental approaches
604 (*e.g.* Fritz et al., 1989; Brunner et al., 2005; Wortmann et al., 2007) but several aspect remain
605 unresolved and, citing Turchyn et al. (2010) "more work is needed".
606
607 *6.2.3 The lateral equivalent of gypsum: microbialites reflecting chemotrophic activity*
608 Recent MSC palaeohydrological models (Krijgsman and Mejers, 2008), predict that during
609 deposition of the Lower Evaporites, the onset of gypsum deposition led to severe density
610 stratification of the Mediterranean water column that resulted in turn in a well mixed, upper water
611 mass underlain by an oxygen-depleted deep water mass. Similar conditions likely existed in the
612 Piedmont Basin during the first MSC stage and may explain why microbialites reflecting the

activity of chemotrophic prokaryotes are the lateral equivalent of bottom-grown selenite beds (Dela Pierre et al., 2011, Fig. 2B). According to field and theoretical models, anoxic sea bottoms would be unfavourable to gypsum formation and preservation, mainly because of low sulphate concentration related in turn to intense bacterial sulphate reduction (*e.g.* Babel, 2007; De Lange and Krijgsman, 2010). On the other hand, this last process produced large amounts of hydrogen sulphide favouring the development of dense chemotrophic microbial mats at the sea floor. Due to the low rate of terrigenous supply, the latters could colonize the sea bottom for a prolonged time interval before their final burial. This circumstance, along with an increased rate of bacterial-mediated carbonate precipitation, allowed the preservation of discrete recognizable beds in the geological record.

7. Conclusions

The carbonate-rich layers of the Pollenzo section straddle the onset of the MSC and provide a detailed record of the environmental changes related to this palaeocenographic event in a sector of the basin where depositional conditions were not suitable for gypsum formation. The integration of field and laboratory data permitted the recognition of the strong difference in the mechanisms responsible for carbonate precipitation before and after the salinity crisis onset.

Dolomite rich-beds actually formed only prior to the onset of the MSC; this interpretation is partially at odds with previous theoretical models (De Lange and Krijgsman, 2010), according to which dolostone layers are the lateral equivalents of the Primay Lower Gypsum beds formed during the first stage of the MSC. The Pollenzo pre-MSC beds are early diagenetic products formed within the sedimentary column in the shallow subsurface within sediments deposited on an oxic sea bottom. Dolomite precipitation was temporarily enhanced by an upward flux of methane-rich fluids possibly sourced by gas-hydrate destabilization.

Conversely, from the onset of the MSC onward, calcite (and aragonite) were the dominant authigenic phases. Microbial-orchestrated carbonate precipitation took place just below the sea

639 bottom, covered by chemotrophic microbial mats dominated by giant sulphide-oxidizing bacteria.
640 The development of these mats was triggered by the establishment of anoxic conditions at the sea
641 bottom (hampering gypsum deposition), in turn related to density stratification of the water column
642 and/or enhanced biological productivity in the water column. The high sulphate concentration in the
643 pore water, related to the presence of concentrated brines and to the physiology of sulphide-
644 oxidizing bacteria (responsible for the continuous "regeneration" of sulphate) were the main factors
645 controlling the mineralogical change from dolomite to calcite. These microbialites do not provide
646 any evidence of sea level lowering at the onset of the MSC as frequently reported, because
647 sulphide-oxidizing bacteria are not light dependent and can live at any depth. Accordingly, the
648 contractional features observed in the sediments, that are commonly regarded as a proof of sea level
649 drop and subaerial exposure, may be ascribed to sediment syneresis due to bacterial EPS
650 degradation in a subaqueous environment.

651 The results of this study highlight how microbial activity can influence the type of
652 authigenic products and the resultant fabrics (dolomite beds *versus* microbialites); moreover, they
653 suggest that care must be taken in the interpretation of the isotope oxygen values in terms of
654 fluctuating salinity conditions of the water mass, with negative values reflecting dilution events and
655 positive ones an increase of the rate of the evaporation. The ^{18}O enrichment of the pre-MSC (early
656 diagenetic) beds does not necessarily reflect the isotopic composition of sea water but rather the
657 contribution of diagenetic fluids in the shallow subsurface. In the same way, the sharp shift towards
658 negative $\delta^{18}O$ values at the onset of MSC may reflect complex fractionation processes operated by
659 sulphate-reducing bacterial communities.

660 Further studies are needed, especially devoted to the characterisation of the biomarker
661 inventory preserved in the carbonates, that could provide more extensive information on the types
662 of microbes involved in carbonate precipitation and on the mutual relationships (if any) with
663 microbes preserved within the gypsum deposited in the shallower part of the Messinian basin(s).
664 This type of approach can contribute to provide information on the changes of microbial

communities at the onset the MSC and on the role played by bacterial activity in modulating evaporite and carbonate sedimentation during the MSC.

Acknowledgements

We thank A. Fusconi for help with UV microscopy and M. Rubbo for advice and criticisms. We also thank the Editor D. Bottjer and two anonymous reviewers for helpful comments and suggestions that greatly improved this manuscript. Research funded by MIUR grants (PRIN-COFIN 2008, Resp. M. Roveri).

References

Arenas, C., Pomar, L., 2010. Microbial deposits in upper Miocene carbonates, Mallorca, Spain. Palaeogeography, Palaeoclimatology, Palaeoecology 297, 465-485.

Bąbel, M., 2007. Depositional environments of a salina type evaporite basin recorded in the Badenian gypsum facies in northern Carpathian Foredeep, In: Schreiber, B. C., Lugli, S., Bąbel, M. (Eds), Evaporites Through Space and Time. Geological Society of London, Special Publication 285, pp.107-142.

Bailey, J.V., Orphan, V.J., Joye, S.B, Corsetti, F., 2009. Chemotrophic microbial mats and their potential for preservation in the rock record. Astrobiology 9, 1-17.

Baker, P.A., Kastner, M., 1981. Constraints on the formation of sedimentary dolomite. Science 213, 214-216.

Barbieri, R., Cavalazzi, B., 2005. Microbial fabrics from Neogene cold seep carbonates, Northern Apennines, Italy. Palaeogeography, Palaeoclimatology, Palaeoecology 227, 143-155.

Baumgartner, L.K., Reid, R. P, Dupraz ,C., Decho, A.V., Buckley, D.H., Spear, J.F., Przekop, K.M., Visscher, P.T., 2006. Sulfate reducing bacteria in microbial mats: changing paradigms, new discoveries. Sedimentary Geology 185, 131-145.

696 Bellanca, A., Caruso, A., Ferruzza, G., Neri, R., Rouchy, J.M., Sprovieri, M., Blanc-Valleron,
697 M.M., 2001. Transition from marine to hypersaline conditions in the Messinian Tripoli Formation
698 from the marginal areas of the central Sicilian Basin. Sedimentary Geology 140, 87-105.
699
700 Bertoni, C., Cartwright, A., 2007. Major erosion at the end of the Messinian salinity crisis: evidence
701 from the Levant basin, eastern Mediterranean. Basin Research 19, 1365-2117.
702
703 Bertotti, G., Mosca, P., 2009. Late orogenic vertical movements within the arc of the SW Alps and
704 Ligurian Alps. Tectonophysics 475, 117-127.
705
706 Bigi, G., Cosentino, D., Parotto, M., Sartori, R., Scandone, P., 1990. Structural Model of Italy:
707 Geodinamic Project: Consiglio Nazionale delle Ricerche, S.EL.CA, scale 1:500,000, sheet 1.
708
709 Blanc-Valleron, M.M., Pierre, C., Caulet, J.P., Caruso, A., Rouchy, J.M., Cespuglio, G., Sprovieri,
710 R., Pestrea, S., Di Stefano, E., 2002. Sedimentary, stable isotope and micropaleontological records
711 of paleoceanographic change in the Messinian Tripoli Formation (Sicily, Italy). Palaeogeography,
712 Palaeoclimatology, Palaeoecology 185, 255-286.
713
714 Boetius, A., Ravenschlag, K., Schubert, C.J., Rickert, D., Widdel, F., Gieseke, A., Amann, R.,
715 Jørgensen, B.B., Witte, U., Pfannkuche, O., 2000. A marine microbial consortium apparently
716 mediating anaerobic oxidation of methane. Nature 407, 623-626.
717
718 Bojanowski, M.J., 2007. Oligocene cold-seep carbonates from the Carpathians and their inferred
719 relation to gas hydrates. Facies 53, 347-360.
720
721 Borowski, W.S., Paull, C.K., Ussler, W., 1999. Global and local variations of interstitial sulfate
722 gradients in deep water, continental margin sediments: sensitivity to underlying methane and gas
723 hydrates. Marine Geology 159, 131-154.
724
725 Braga, J.C., Martín, J.M., Riding R., Aguirre J., Sánchez-Almazo I. M., Dinarès-Turell J., 2006.
726 Testing models for the Messinian salinity crisis: the Messinian record in Almería, SE Spain.
727 Sedimentary Geology 188-189, 131-154.
728

729 Brunner, B., Bernasconi, S.M., Kleikemper, J., Schroth, M.H., 2005. A model for oxygen and sulfur
730 isotope fractionation in sulfate during bacterial sulfate reduction processes. Geochimica et
731 Cosmochimica Acta 69, 4773-4785.
732
733 Campbell, K. A., 2006. Hydrocarbon seep and hydrothermal vent paleoenvironments and
734 paleontology: past developments and future research directions. Palaeogeography,
735 Palaeoclimatology,. Palaeoecology 232, 362-407.
736
737 Cavagna, S., Clari, P., Martire, L., 1999. The role of bacteria in the formation of cold seep
738 carbonates: geological evidence from Monferrato (Tertiary, NW Italy). Sedimentary Geology 126,
739 253-270.
740
741 CIESM, 2008. The Messinian Salinity Crisis from mega-deposits to microbiology – A consensus
742 report. CIESM Workshop Monographs N° 33, F. Briand Eds, Monaco, pp.168.
743
744 Cita, M.B., Wright, R.C., Ryan, W.B.F., Longinelli, A., 1978. Messinian paleoenvironments, In:
745 Hsü, K.J., Montadert, L. et al. (Eds.), Initial Reports of the Deep Sea Drilling Project 42. U.S.
746 Government Printing Office, Washington D.C, pp. 1003-1035.
747
748 Clauzon, G., Suc, J.P., Gautier, F., Berger, A., Loutre, M.F., 1996. Alternative interpretation of the
749 Messinian salinity crisis: controversy resolved? Geology 24, 363-366.
750
751 Compton, J. S., 1988, Degree of supersaturation and precipitation of organogenic dolomite:
752 Geology 16, 318-321.
753
754 Dählmann, A., De Lange, G.J., 2003. Fluid-sediment interactions at Eastern Mediterranean mud
755 volcanoes: a stable isotope study from ODP Leg 160. Earth and Planetary Science Letters 212, 377-
756 391.
757
758 De Lange, G. J., Krijgsman, W., 2010. Messinian salinity crisis: a novel unifying shallow
759 gypsum/deep dolomite formation mechanism. Marine Geology 275, 273-277.
760
761 Decima, A., McKenzie, J.A., Schreiber, B.C., 1988. The origin of ‘evaporative’ limestones: an
762 example from the Messinian of Sicily (Italy). Journal of Sedimentary Petrology 58, 256-272.

763
764 Dela Pierre, F., Festa, A., Irace, A., 2007. Interaction of tectonic, sedimentary and diapiric
765 processes in the origin of chaotic sediments: an example from the Messinian of Torino Hill
766 (Tertiary Piedmont Basin, northwestern Italy). Geological Society of America Bulletin 119, 1107-
767 1119.
768
769 Dela Pierre, F., Martire, L., Natalicchio, M., Clari, P.A., Petrea, C., 2010. Authigenic carbonates in
770 the upper Miocene sediments of the Tertiary Piedmont Basin (NW Italy): vestiges of an ancient gas
771 hydrate stability zone? Geological Society of America Bulletin 122, 994-1010.
772
773 Dela Pierre, F., Bernardi, E., Cavagna, S., Clari, P, Gennari, R., Irace, A., Lozar, F., Lugli, S.,
774 Manzi, V., Natalicchio, M., Roveri, M., Violanti, D., 2011. The record of the Messinian salinity
775 crisis in the Tertiary Piedmont Basin (NW Italy): The Alba section revisited. Palaeogeography,
776 Palaeoclimatology, Palaeoecology 310, 238-255.
777
778 Dewhurst, D. N., Cartwright, J. A., Lonergan, L., 1999. The development of polygonal fault
779 systems by syneresis of colloidal sediments. Marine and Petroleum Geology 16, 793-810.
780
781 D'Hondt, S., Rutherford, S., Spivack, A.J., 2002. Metabolic activity of subsurface life in deep-sea
782 sediments. Science 295, 2067-2070.
783
784 Dupraz, C., Visscher, P.T. 2005. Microbial lithification in marine stromatolites and hypersaline
785 mats. Trends in Microbiology 13, 429-438.
786
787 Dupraz, C., Reid, R.P., Braissant, O., Decho, A.W., Norman, R.S., Visscher, P.T., 2009. Processes
788 of carbonate precipitation in modern microbial mats. Earth Science Reviews 96, 141-162.
789
790 Esteban, M., 1979. Significance of Upper Miocene coral reefs of the western Mediterranean.
791 Palaeogeography Palaeoclimatology Palaeoecology 29, 169-188.
792
793 Feldmann, M., Mc Kenzie, J.A., 1997. Messinian stromatolite-thrombolite associations, Santa Pola,
794 SE Spain: an analogue for the Paleozoic? Sedimentology 44, 893-914.
795

796 Fossing, H., Gallardo,V.A., Jørgensen, B.B., Hüttel, M., Nielsen, L.P., Schulz, H., Canfield, D.E.,
797 Forster, S., Glud, R.N., Gundersen, J.K., Küver, J., Ramsing, N.B., Teske, A., Thamdrup, B.,
798 Ulloa, O., 1995. Concentration and transport of nitrate by the mat-forming sulphur bacterium
799 *Thioploca*. Nature 374, 713-715.
800
801 Fossing, H., Felderman, T.G., Berg, P., 2000. Sulphate reduction and methane oxidation in
802 continental margin sediments influenced by irrigation (South-East Atlantic off Namibia)
803 Geochimica et Cosmochimica Acta 64, 897-900.
804
805 Fritz, P., Basharmal, G.M., Drimmie, R.J., Ibsen, J and Qureshi, R.M., 1989. Oxygen isotope
806 exchange between sulphate and water during bacterial reduction of sulphate. Chemical Geology,
807 Isotope Geoscience Section 79, 99-105.
808
809 Gallardo, V.A. 1977. Large benthic microbial communities in sulphide biota under Peru-Chile
810 subsurface counter current. Nature 286, 331-332.
811
812 Garcia-Veigas, J., Orti, F., Rosell, L., Ayora, C., Rouchy, J.M., Lugli, S., 1995. The Messinian salt
813 of the Mediterranean: Geochemical study of the salt from the Central Sicily Basin and comparison
814 with the Lorca Basin (Spain). Bulletin de la Société Géologique de la France 166, 699-710.
815
816 Guido, A., Jacob, J., Gautret, P., Laggoun-Defarge, F., Mastandrea, A., Russo, F., 2007. Molecular
817 fossils and other organic markers as paleoenvironmental indicators of the Messinian Calcare di
818 Base Formation: Normal versus stressed marine deposition (Rossano Basin, northern Calabria,
819 Italy). Palaeogeography, Palaeoclimatology, Palaeoecology 255, 265-283.
820
821 Hendry, J.P., Pearson, M.J., Trewin, N.H., Fallick, A.E., 2006. Jurassic septarian concretions from
822 NW Scotland record interdependent bacterial, physical and chemical processes of marine mudrock
823 diagenesis. Sedimentology 53, 537-565.
824
825 Hsü, K.J., Cita, M.B., Ryan, W.B.F., 1973. The origin of the Mediterranean evaporites, In: Ryan,
826 W.B.F., Hsü, K.J., et al. (Eds.), Initial Report of Deep Sea Drilling Program 13. U.S. Government
827 Printing Office, Washington DC, pp. 1203-1231.
828
829 Kastner, M., 1984. Sedimentology: control of dolomite formation. Nature 5985, 410-411.

Krijgsman, W., Hilgen, F.J., Raffi, I., Sierro, F.J., Wilson, D.S., 1999. Chronology, causes and progression of the Messinian salinity crisis. Nature 400, 652-655.

Krijgsman, W., Blanc-Valleron, M.M., Flecker, R., Hilgen, F.J., Kouwenhoven, T.J., Merle, D., Orszag-Sperber, F., Rouchy, J.M., 2002. The onset of the Messinian salinity crisis in the Eastern Mediterranean (Pissouri Basin, cyprus). Earth and Planetary Science Letters 194, 299-310.

Krijgsman, W., Meijer P.T., 2008. Depositional environments of the Mediterranean "Lower Evaporites" of the Messinian salinity crisis: constraints from quantitative analyses. Marine Geology 253, 73-81.

Irace, A., Clemente, P., Natalicchio, M., Ossella, L., Trenkwalder, S., De Luca, D. A., Mosca, P., Piana, F., Polino, R., Violanti, D., 2010. Geologia e idrostratigrafia profonda della Pianura Padana occidentale: La Nuova Lito Firenze, pp. 110, ISBN 978-88-904554-0-7.

Irwin, H., Cultis, C., Coleman, M., 1977. Isotopic evidence for source of diagenetic carbonates formed during burial of organic-rich sediments. Nature 269, 209-213.

Jannasch, H.W., Nelson, D.C., Wirsen, C.O., 1989. Massive natural occurrence of unusually large bacteria (*Beggiatoa* spp.) at a hydrothermal deep-sea vent site. Nature 342, 834-836.

Jørgensen, B. B., Kasten, S., 2006. Sulfur cycling and methane oxidation. In: Schulz, H.D, Zabel, M. (Eds.), Marine Geochemistry, 2nd ed. Springer, Berlin, 271-309.

Larkin, J., Aharon, P., Henk, M.C., 1994. *Beggiatoa* in microbial mats at hydrocarbon vents in the Gulf of Mexico and Warm Mineral Springs, Florida. Geo-Marine Letters 14, 97-103.

Lloyd, R.M., 1968. Oxygen isotope behavior in the sulfate-water system. Journal of Geophysical Research 73, 6099-6110.

Lofi, J., Sage, F., Déverchère, J., Loncke, L., Maillard, A., Gallier, V., Thinon, I., Gillet, H., Guennoc, P., Gorini, C., 2011. Refining our knowledge of the Messinian salinity crisis in the offshore domain through multi-site seismic analysis. Bulletin Société Géologique de France, 182, 163-180.

865

866 Lozar, F., Violanti, D., Dela Pierre, F., Bernardi, E., Cavagna, S., Clari P., Irace, A., Martinetto, E.,
867 Trenkwalder, S., 2010. Calcareous nannofossils and foraminifers herald the Messinian salinity
868 crisis: the Pollenzo section (Alba, Cuneo; NW Italy). Geobios 43, 21-32.
869
870 Lugli, S., Manzi, V., Roveri, M., Schreiber, B.C., 2010. The Primary Lower Gypsum in the
871 Mediterranean: a new facies interpretation for the first stage of the Messinian salinity crisis.
872 Palaeogeography, Palaeoclimatology, Palaeoecology 297, 83-99.
873
874 Manzi, V., Roveri, M., Gennari, R., Bertini, A., Biffi, U., Giunta, S., Iaccarino, S., Lanci, L., Lugli,
875 S., Negri, A., Riva, A., Rossi, M.E., Taviani, M., 2007. The deep-water counterpart of the
876 Messinian Lower Evaporites in the Apennine foredeep: the Fanantello section (Northern Apennines,
877 Italy). Palaeogeography, Palaeoclimatology, Palaeoecology 251, 470-499.
878
879 Manzi, V., Lugli, S., Roveri, M., Schreiber, B.C., Gennari, R., 2011. The Messinian "Calcare di
880 Base" (Sicily, Italy) revisited. Geological Society of America Bulletin 123, 347-370.
881
882 Martire, L., Natalicchio, M., Petrea, C., Cavagna, S., Clari, P., Dela Pierre F., 2010. Petrographic
883 evidence of the past occurrence of gas hydrates in the Tertiary Piedmont Basin (NW Italy). Geo-
884 Marine Letters 30, 461-476.
885
886 Mc Crea, J.M., 1950. The isotopic chemistry of carbonates and a paleotemperature scale. Journal of
887 Chemical Physics 18, 849-857.
888
889 Mc Kenzie, J.A., Jenkyns, H.C., Bennet, G.G., 1979. Stable isotope study of the cyclic diatomite
890 claystones from the Tripoli Formation, Sicily: a prelude to the Messinian Salinity crisis.
891 Palaeogeography, Palaeoclimatology, Palaeoecology 29, 125-141.
892
893 Meister, P., McKenzie, J.A., Vasconcelos, C., Bernasconi, S., Frank, M., Gutjahr, M., Schrag, D.P.,
894 2007. Dolomite formation in the dynamic deep biosphere, results from the Peru Margin, OPD Leg
895 201. Sedimentology 54, 1007-1032.
896

Meister, P., Bernasconi, S.M, Vasconcelos, C., McKenzie, J.A., 2008. Sea level changes control diagenetic dolomite formation in hemipelagic sediments of the Peru Margin. Marine Geology 252, 166-173.

Møller, M.M., Nielsen, L.P., Jørgensen, B.B., 1985. Oxygen responses and mat formation by *Beggiatoa* spp. Applied Environmental Microbiology 50, 373–382.

Mosca, P., Polino, R., Rogledi, S., Rossi, M., 2009. New data for the kinematic interpretation of the Alps–Apennines junction (Northwestern Italy). International Journal of Earth Sciences 99, 833-429.

Mussman, M., Schulz, H.N., Strotmann, B., Kyær, T., Nielsen, L.P., Rossellò-Mora, R.A., Amann, R.I., Jørgensen, B.B., 2003. Phylogeny and distribution of nitrate-storing *Beggiatoa* spp. in coastal marine sediments. Environmental Microbiology 5, 523-533.

Natalicchio, M., Birgel, D., Dela Pierre, F., Martire, L., Clari, P., Spötl, C., Peckmann, J., 2012. Polyphasic carbonate precipitation in the shallow subsurface: insights from microbially-formed authigenic carbonate beds in upper Miocene sediments of the Tertiary Piedmont Basin (NW Italy). Palaeogeography, Palaeoclimatology, Palaeoecology 329-330, 158-172.

Oliveri, E., Neri, R., Bellanca, A., Riding, R., 2010. Carbonate stromatolites from a Messinian hypersaline setting in the Caltanissetta Basin, Sicily: petrographic evidence of microbial activity and related stable isotope and rare earth element signatures. Sedimentology 57, 142-161.

Orszag-Sperber, F., Caruso, A., Blanc-Valleron, M.M., Merle, D., Rouchy, J.M., 2009. The onset of the Messinian salinity crisis: insights from Cyprus sections. Sedimentary Geology 217, 52-64.

Palacios, C., Zbinden, M., Pailleret, M., Gaill, F., Lebaron, P., 2009. Highly similar prokaryotic communities of sunken wood at shallow and deep-sea sites across the Oceans. Microb. Ecol. 58, 737-752

Panieri, G., Lugli, S., Manzi, V., Roveri, M., Schreiber, C.B., Palinska, K.A., 2010. Ribosomal RNA gene fragments from fossilized cyanobacteria identified in primary gypsum from the late Miocene, Italy. Geobiology 8, 101-111.

931
932 Peckmann, J., Thiel, V., 2004. Carbon cycling at ancient methane-seeps. Chemical Geology, 205,
933 443-467.
934
935 Peckmann, J., Thiel, V., Reitner, J., Taviani, M. Aharon, P., Michaelis, W., 2004. A microbial mat
936 of a large sulfur bacterium preserved in a Miocene methane-seep limestones. Geomicrobiology
937 Journal 21, 247-255.
938
939 Petrash, D.A., Murray, K.G., Lalonde, S.V., Pecotis, E., Konhauser, K.O, 2012. Dynamic controls
940 on accretion of modern gypsum-dominated thrombolites, Los Roques, Venezuela. Sedimentary
941 Geology, 245-246, 29-47.
942
943 Pierre, C., Rouchy, J.M., 2004. Isotopic compositions of diagenetic dolomites in the Tortonian
944 marls of the Western Mediterranean margins: evidence of past gas hydrate formation and
945 dissociation. Chemical Geology 205, 469-484.
946
947 Raiswell, R., 1987. Non–steady state microbial diagenesis and the origin of carbonate concretion
948 and nodular limestones. In Marshall, J.D., Ed., Diagenesis of Sedimentary Sequences, Geological
949 Society of London, Special Publication 36, pp. 41-54.
950
951 Raiswell, R., Fisher, Q.J., 2000. Carbonate concretions: a review of growth mechanisms and their
952 influence on chemical and isotopic composition. Journal of the Geological Society 157, 239-257.
953
954 Raiswell, R., Fisher, Q.J., 2004. Rates of carbonate cementation associated with sulphate reduction
955 in DSDP/ODP sediments: implications for the formation of concretions. Chemical Geology 211,
956 71-85.
957
958 Riding, R., Braga, J. C., Martín, J. M., Sánchez-Almazo, I. M., 1998. Mediterranean Messinian
959 Salinity Crisis: constraints from a coeval marginal basin, Sorbas, southeastern Spain. Marine
960 Geology 146, 1-20.
961
962 Roberts, H.H., Aharon, P., 1994. Hydrocarbon-derived carbonate buildups of the northern Gulf of
963 Mexico continental slope: a review of submersible investigations. Geo-Marine Letters 14, 135-148.
964

965 Rossi, M., Mosca, P., Polino, R., Biffi, U., 2009. New outcrop and subsurface data in the Tertiary
966 Piedmont Basin (NW Italy): unconformity bounded stratigraphic units and their relationships with
967 basin modification phases. Rivista Italiana di Paleontologia e Stratigrafia 115, 305-335.
968
969 Rouchy, J. M., Caruso, A., 2006. The Messinian Salinity Crisis in the Mediterranean basin: a
970 reassessment of data and an integrated scenario. Sedimentary Geology 188-189, 35-67.
971
972 Rouchy J.M., Monty C.L., 1981. Stromatolites and cryptalgal laminites associated with Messinian
973 gypsum of Cyprus. In: Monty C.L. (Ed.), Phanaerozoic stromatolites. Springer Verlag, pp. 155-178.
974
975 Rouchy, J.M., Taberner, C., Blanc-Valleron, M.M., Sprovieri, R., Russell, M., Pierre, C., Di
976 Stefano, E., Pueyo, J.J., Caruso, A., Dinares, J., Gomis-Coll, E., Cespuglio, G.,Wolff, G.,
977 Ditchfield, P., Santisteban, C., Pestrea, S., Combourieu-Nebout, N., Santisteban, S., Grimalt, J.O.,
978 1998. Sedimentary and diagenetic markers of the restriction in a marine basin: the Lorca Basin (SE
979 Spain) during the Messinian. Sedimentary Geology 121, 23-55.
980
981 Roveri, M., Lugli, S., Manzi, V., Schreiber, B.C., 2008. The Messinian Sicilian stratigraphy
982 revisited: new insights for the Messinian Salinity Crisis. Terra Nova 20, 483-488.
983
984 Roveri, M., Gennari, R., Lugli, S., Manzi, V., 2009. The Terminal Carbonate Complex: the record
985 of sea-level changes during the Messinian salinity crisis. Geoacta 8, 63-77.
986
987 Ryan, W.B.F., 1976. Quantitative evaluation of the depth of the western Mediterranean before,
988 during and after the late Miocene salinity crisis. Sedimentology 23, 791-813.
989
990 Sahling, H., Rickert, D., Raymond, W. L., Linke, P., Suess, E., 2002. Macrofaunal community
991 structure and sulfide flux at gas hydrate deposits from the Cascadia convergent margin, NE Pacific.
992 Marine Ecology Progress Series 231, 121-138.
993
994 Sánchez-Román, M., McKenzie, J. A., Rebello Wagener, A. de L., Rivadeneyra, M., Vasconcelos,
995 C., 2009. Presence of sulfate does not inhibit low-temperature dolomite precipitation. Earth and
996 Planetary Science Letters 285, 131-139.
997

998 Sass, E., Bein, A., Almogi-Labin, A., 1991. Oxygen-isotope composition of diagenetic calcite in
999 organic-rich rocks: evidence for ^{18}O depletion in marine anaerobic pore water. Geology 19, 839-
1000 842.

1001

1002 Schreiber, B.C., Friedman, G.M., 1976. Depositional environments of Upper Miocene (Messinian)
1003 evaporites of Sicily as determined from analysis of intercalated carbonates. Sedimentology 23, 255-
1004 270.

1005

1006 Schulz, H.N., Brinkhoff, T. Ferdelman, G., Hernanndez Marine, M., Teske, A., Jørgensen, B.B.,
1007 1999. Dense populations of a giant sulfur bacterium in Namibian shelf sediments. Science 284, 493-
1008 495.

1009

1010 Schulz, H.N., Jørgensen, B.B., 2001. Big bacteria. Annuual Review of Microbiology. 55, 105-37.

1011

1012 Sturani, C., 1973. A fossil eel (*Anguilla* sp.) from the Messinian of Alba (Tertiary Piedmont Basin).
1013 Palaeoenvironmental and palaeogeographic implications, In: Messinian events in the
1014 Mediterranean. K. Nederl. Akad. Wetensch., Amsterdam, pp. 243-255.

1015

1016 Sturani, C., 1976. Messinian facies in the Piedmont basin. Memorie della Società Geologica Italiana
1017 16, 11-25.

1018

1019 Sturani, C., Sampò, M., 1973. Il Messiniano inferiore in facies diatomitica nel Bacino Terziario
1020 Piemontese. Memorie della Società Geologica Italiana 12, 335-338.

1021

1022 Teichert, B. M. A., Bohrmann, G., Suess, E., 2005. Chemoherms on Hydrate Ridge - Unique
1023 microbially-mediated carbonate builups growing into the water column. Palaeogeography,
1024 Palaeoclimatology, Palaeoecology 227, 67-85.

1025

1026 Treude, T., Krüger, M., Boetius, A., Jørgensen, B.B., 2005. Environmental control on anaerobic
1027 oxidation of methane in the gassy sediments of Eckernförde Bay (German Baltic). Limnology and
1028 Oceanography 50, 1771-1786.

1029

1030 Treude, T., Smith, C.R., Wenzhöfer, F., Carney, E., Bernardino, A.F., Hannides, A.K., Krüger, M.,
1031 Boetius, A., 2009. Biogeochemistry of a deep-sea whale fall: sulfate reduction, sulphide efflux and
1032 methanogenesis. Marine Ecology Progresse Series 382, 1-21.
1033
1034 Turchyn A. V., Brüchert, V., Lyons, T.W., Engel, G.S., Balci, N., Schrag, D.P, Brunner, B., 2010 .
1035 Kinetic oxygen isotope effects during dissimilatory sulfate reduction: A combined theoretical and
1036 experimental approach. Geochimica et Cosmochimica Acta 74, 2011-2024.
1037
1038 Ussler III, W., Paull, C.K., 2008. Rates of anaerobic oxidation of methane and authigenic carbonate
1039 mineralization in methane-rich deep-sea sediments inferred from models and geochemical profiles.
1040 Earth and Planetary Science Letters 266, 271-28.
1041
1042 Vai, G.B., Ricci Lucchi, F., 1977. Algal crusts, autochtonous and clastic gypsum in a cannibalistic
1043 evaporite basin; a case history from the Messinian of Northern Apennine. Sedimentology 24, 211-
1044 244.
1045
1046 Vasconcelos, C., Mc Kenzie, J.A., Bernasconi, S., Grujic, D., Tien, A.J., 1995. Microbial mediation
1047 as a possible mechanism for natural dolomite formation at low temperatures. Nature 377, 220-222.
1048
1049 Wacey, D., Wright, D.T., Boyce, A.J., 2008. A stable isotope study of microbial dolomite formation
1050 in the Coorong Region, South Australia. Chemical Geology 244, 155-174.
1051
1052 Wortmann, U.G., Chernyavsky B., Bernasconi, S.M., Brunner, B., Boettcher, M.E., Swart, P.K.,
1053 2007. Oxygen isotope biogeochemistry of pore water sulfate in the deep biosphere: dominance of
1054 isotope exchange reactions with ambient water during microbial sulfate reduction (ODP Site 1130).
1055 Geochimica et Cosmochimica Acta 71, 4221–4232.
1056
1057 Wright, D.T., Oren, A., 2005. Nonphotosynthetic bacteria and the formation of carbonates and
1058 evaporites through time. Geomicrobiology Journal 22, 27-53.
1059
1060 Ziegenbalg, S.B., Brunner, B., Rouchy, J.M., Birgel, D., Pierre, C., Böttcher, M.E., Caruso, A.,
1061 Immenhauser, A., Peckmann, J., 2010. Formation of secondary carbonates and native sulphur-rich
1062 Messinian strata, Sicily. Sedimentary Geology 227, 37-50.
1063

1064 Ziegenbalg, S.B., Birgel, D., Hoffmann-Sell, L., Pierre, C., Rouchy, J.M., Peckmann, J., 2012.
1065 Anaerobic oxidation of methane in hypersaline Messinian environments revealed by ^{13}C-depleted
1066 molecular fossils. Chemical Geology 292-293, 140-148.
1067
1068
1069
1070

Figure captions

Fig. 1. A) Structural sketch of NW Italy (modified from Bigi et al., 1990). The asterisk shows the location of the Pollenzo section. TH: Torino Hill; MO: Monferrato: AM: Alto Monferrato; BG: Borbera-Grue; VVL: Villalevernia-Varzi Line; SVZ: Sestri-Voltaggio zone; IL: Insubric Line. B) Regional section in a N-S direction (redrawn after Bertotti and Mosca, 2009; Mosca et al., 2009). Location in Fig. 1A.

Fig. 2. A**)** Schematic cross section, flattened at the base of the Pliocene, showing the relationships among the Messinian units. PLG: Primary Lower Gypsum unit; RLG: Resedimented Lower Gypsum unit; MES: Messinian erosional surface; SKB: Sturani key-bed; CRB: carbonate-rich beds (from Dela Pierre et al, 2011). Not to scale. B) Stratigraphic model of the MSC record of Alba along a SW-NE cross section flattened at the base of the Pliocene. The location of the Pollenzo section is shown. The carbonate-rich beds discussed in the text are marked in yellow (from Dela Pierre et al., 2011). Abbrevietions as in Fig. 2A. The trace of the cross section is shown in Fig. 1A.

Fig. 3. The Pollenzo section (left) and detail of the upper part of the Sant'Agata Fossili Marls (right). ICP data (total carbonates, dolomite and calcite) and stable isotope data of pre-MSC and MSC cycles are shown. SKB: Sturani-key bed; RLG: Resedimented Lower Gypsum unit; AAF: Argille Azzurre Formation; hb: hemi-ellipsoidal body. Chrono-biostratigraphic data and distribution of foraminifers and calcareous nannofossils are from Lozar et al. (2010) and Dela Pierre et al., (2011).

Fig. 4. The upper part of the Sant'Agata Fossili Marls at Pollenzo; the carbonate-rich beds discussed in the text are shown. From this perspective view bed *a* is not visible. SAF: Sant'Agata Fossili Marls; PLG: Primary Lower Gypsum unit.

1097 **Fig. 5.** Pre-MSC beds. A) Outcrop view of bed *a*. Note the sharp lower and upper boundaries. B)
1098 Polished slab of bed *a*. Burrows (arrows) can be recognised. C) Photomicrograph (plane light) of
1099 bed *c*; silt-sized terrigenous grains and burrows can be recognised. D) SEM image of a slightly
1100 etched broken chip of bed *a*. Rhombohedric dolomite crystals are clearly recognisable. E) SEM
1101 image of a slightly etched broken chip of bed *d.* Pyrite framboids and dolomite crystals are visible.
1102
1103 **Fig. 6**. MSC beds. A) Outcrop view of the uppermost part of the Sant'Agata Fossili Marls. Beds *e*, *f*
1104 and *g* and the hemi-ellipsoidal body (hb) can be recognised. B) Photomicrograph (plane light) of
1105 bed *e*, showing rounded clasts encircled by circumgranular cracks (arrows). C) Polished slab of bed
1106 *f*, showing whitish and grey laminae. Some cracks can be recognised within whitish laminae
1107 (arrows). D) Photomicrograph (plane light) of bed *f*, showing the alternation of carbonate and
1108 terrigenous-rich laminae. Note the contractional cracks in the carbonate laminae. E)
1109 Photomicrograph in epifluorescence of bed *f*. Note the stronger fluorescence of the carbonate
1110 lamina (lower part). Filaments (arrows) can be seen in the carbonate lamina.
1111
1112 **Fig. 7**. MSC beds. A) Photomicrograph (plane light) of bed *g*. Note the thin lamination and the
1113 black filaments (arrows) underlined by a concentration of pyrite framboids. B) SEM images of a
1114 broken chip of bed *f* showing globular calcite crystals with a central hollow. C) Photomicrograph
1115 (plane light) of bed *g* with a detail of a filament. D) Photomicrograph in epifluorescence of the same
1116 filament of Fig. 7C. Note its different epifluorescence with respect to the surrounding matrix and
1117 the abundant pyrite framboids preserved within it.
1118
1119 **Fig. 8**. The hemi-ellipsoidal body. A) Outcrop view. B) Polished slab of a sample collected in the
1120 upper part of the body; note the wrinkled lamination. C) and D) Photomicrographs in plane light
1121 and in epifluorescence of some filaments. Note in D) the stronger epifluorescence of the calcite
1122 infilling of a large filament. E) Photomicrograph (plane light) of curved filaments surrounded by

1123 fringing aragonite (arrows). The central portion of the intergranular voids is filled with calcite (cc).
1124 F) SEM image of a slightly etched broken chip showing slightly curved calcite filaments,
1125 surrounded by aragonite fringes (ar).
1126
1127 **Fig. 9.** The hemi-ellipsoidal body: pyrite framboids growing on aragonite fringes.
1128
1129 **Fig. 10.** Genesis of the pre-MSC carbonate-rich beds at the sulphate-methane interface (SMI).
1130 A) During formation of beds *a* and *b*, bacterial sulphate reduction was coupled to anaerobic
1131 oxidation of methane (AOM); methane derived (at least in part) from gas hydrate (GH)
1132 destabilization. B) Dolomite precipitation in beds *c* and *d* was induced by bacterial sulphate
1133 reduction alone, fuelled by organic matter oxidation. In these beds the dolomite content is lower
1134 than in beds *a* and *b*. Depth of the SMI below the sea floor was probably of few metres and was
1135 shallower for beds *a* and *b*, due to the larger supply of methane from below.
1136
1137 **Fig. 11.** Genesis of the MSC carbonate-rich-beds. Carbonate precipitation was triggered by
1138 bacterial sulphate reduction in organic-matter-rich anoxic sediments immediately below the sea
1139 floor; the latter was covered by filamentous sulphide-oxidizing bacteria (F). Since sulphate was not
1140 completely consumed, calcite was favoured. Dolomite could precipitate only later at the sulphate-
1141 methane-interface (SMI). For further detail see text.
1142
1143 **Fig. 12.** Formation of laminated carbonate beds.
1144 A) A mat of filamentous sulphide-oxidizing bacteria developed at the sea floor, sustained by a
1145 sulphide flux sourced by bacterial sulphate reduction working in the shallow subsurface; here active
1146 calcite precipitation took place. B) A layer of organic-matter-poor terrigenous sediment buried the
1147 chemotrophic mat, slowing down the activity of sulphate-reducing bacteria. C) After the terrigenous
1148 influx ceased, the activity of sulphate-reducing bacteria resumed, focused in organic-rich layers (a

buried chemotrophic mat in this example). The ensuing calcite (and pyrite) precipitation preserved the dead bacterial filaments, while a new chemotrophic mat developed on the aggraded sea floor. Calcite was followed by dolomite precipitation (see Fig. 11). For further detail, see text.

Table 1. ICP data of pre-MSC (light grey shadow) and MSC (dark grey shadow) sediments; h.m: homogeneous marl; l.s.: laminated shale: T.C: total carbonate.

Table 2. Percentage of dolomite and calcite with respect to the total carbonate (T.C.) content in the pre-MSC (light grey shadow) and MSC (dark grey shadow) carbonate-rich beds.

Table 3. Stable isotope data of pre-MSC (light grey shadow) and MSC (dark grey shadow) sediments. Carbonate-rich beds are in bold. Hem. body: hemi-ellipsoidal body.

Figure
Click here to download high resolution image

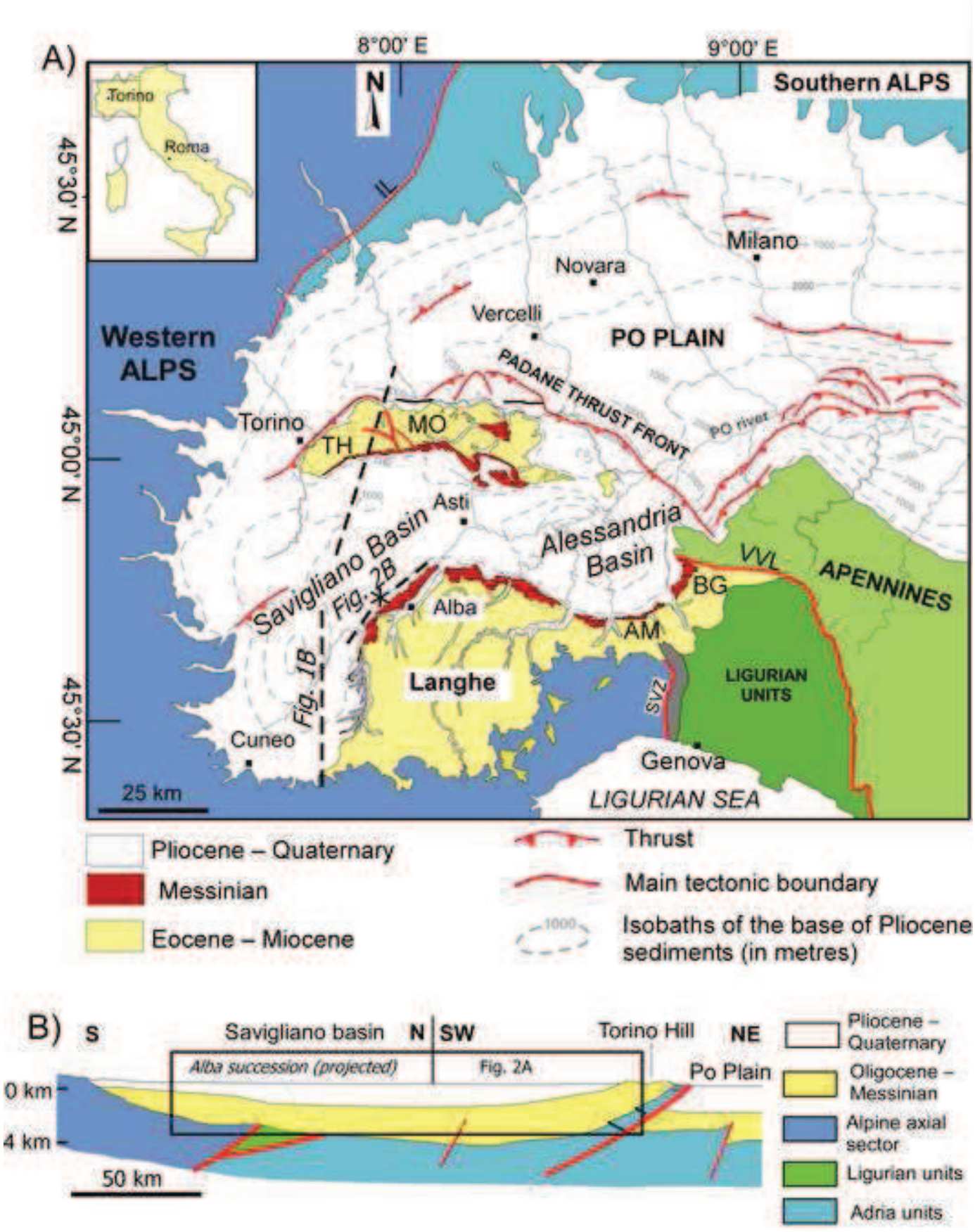

Dela Pierre et al. Fig. 1

Figure
Click here to download high resolution image

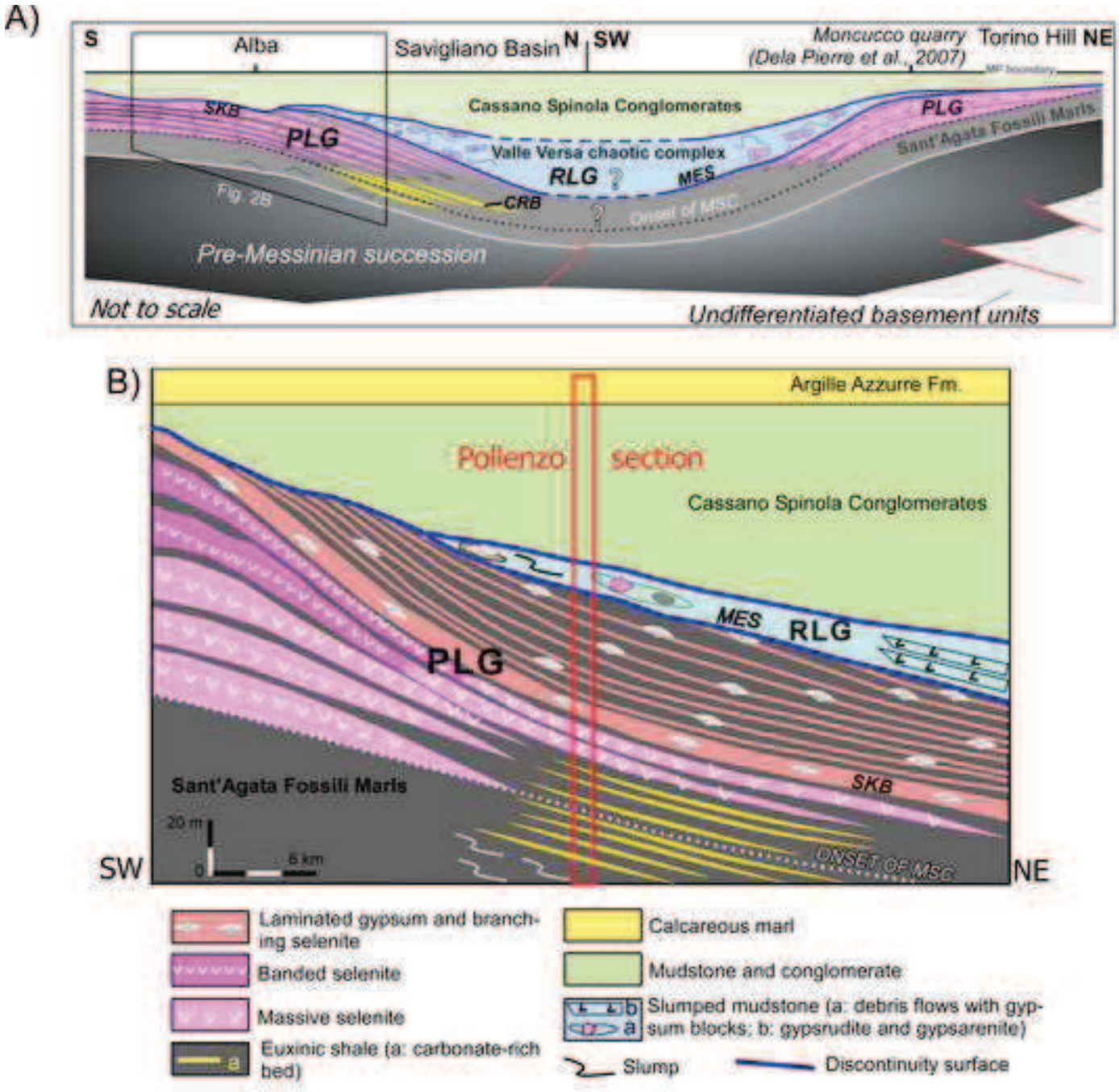

Dela Pierre et al. Fig. 2

Figure
Click here to download high resolution image

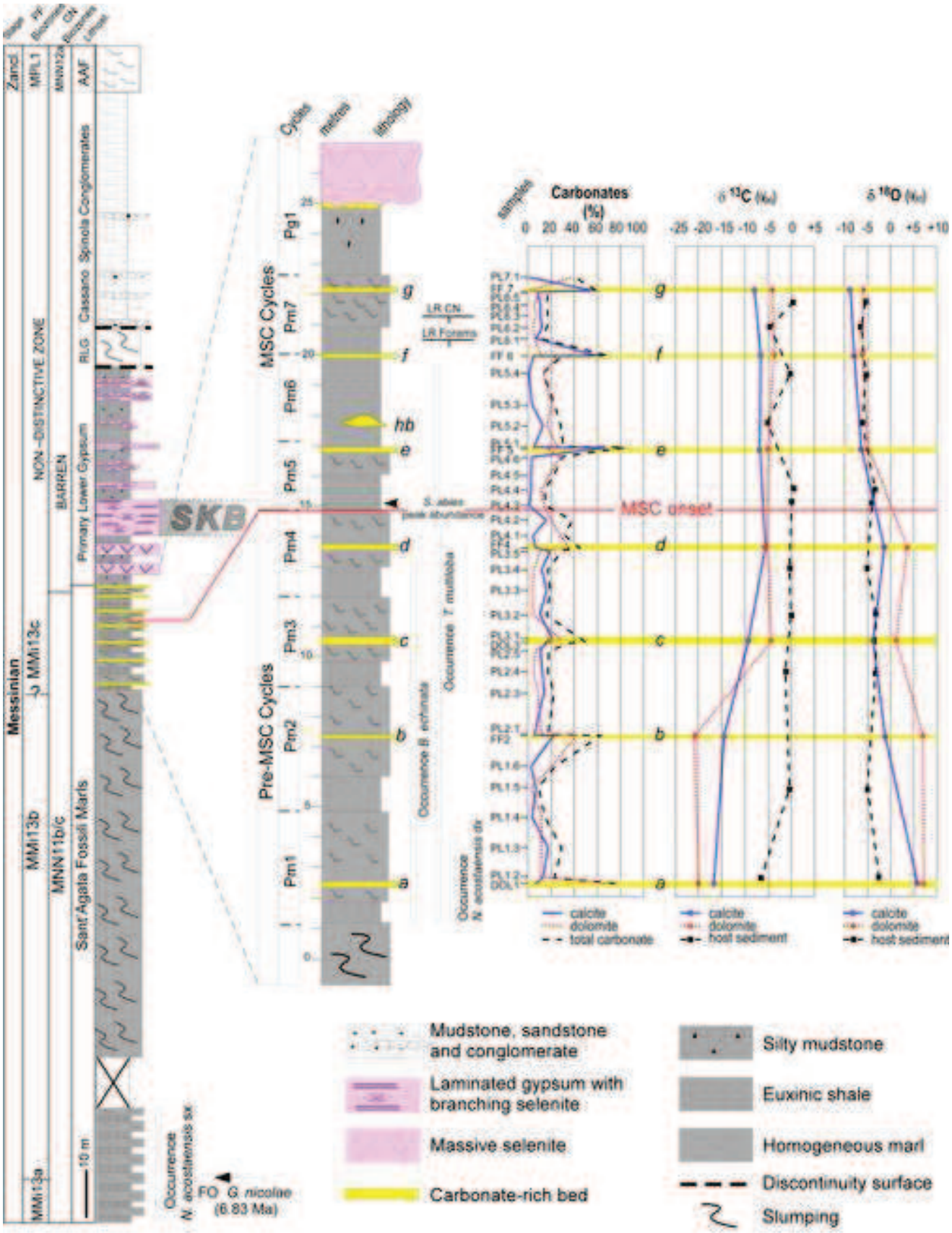

Dela Pierre et al., Fig. 3

Figure
Click here to download high resolution image

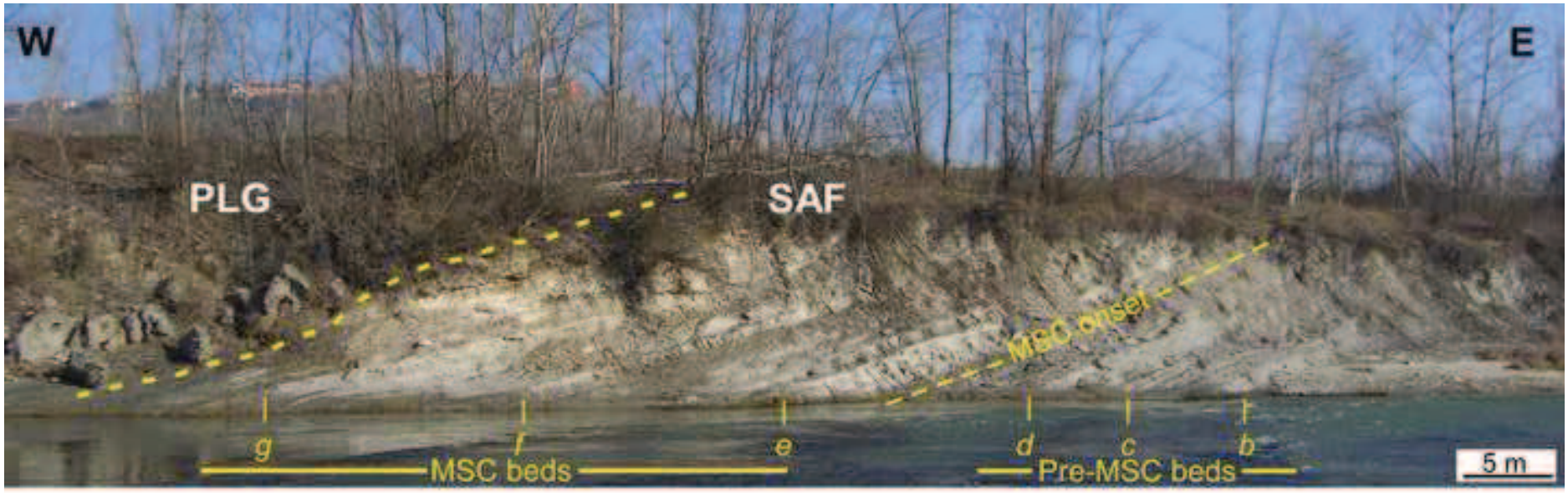

Dela Pierre et al. Fig. 4

Figure
Click here to download high resolution image

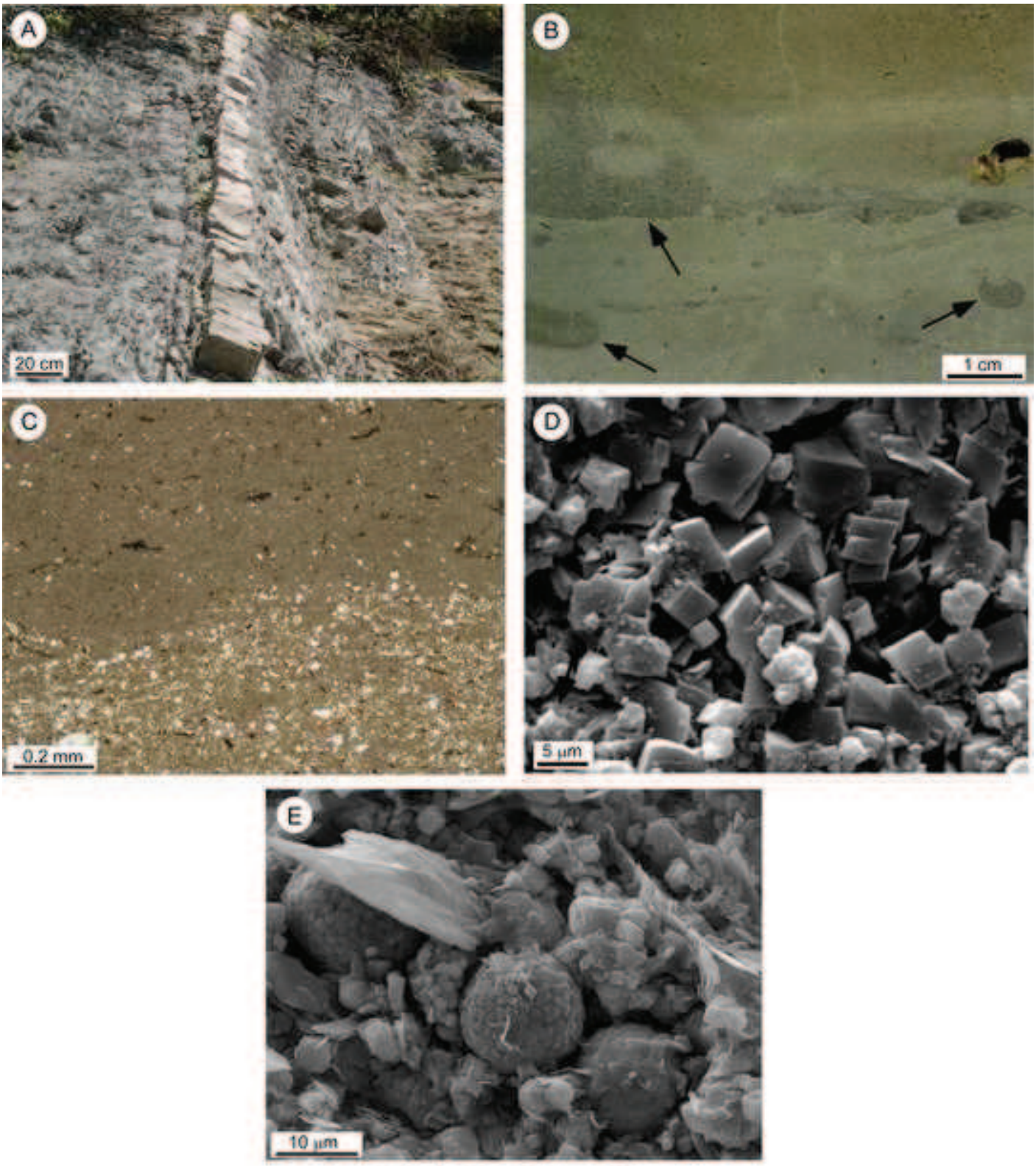

Dela Pierre et al., Fig. 5

Figure
Click here to download high resolution image

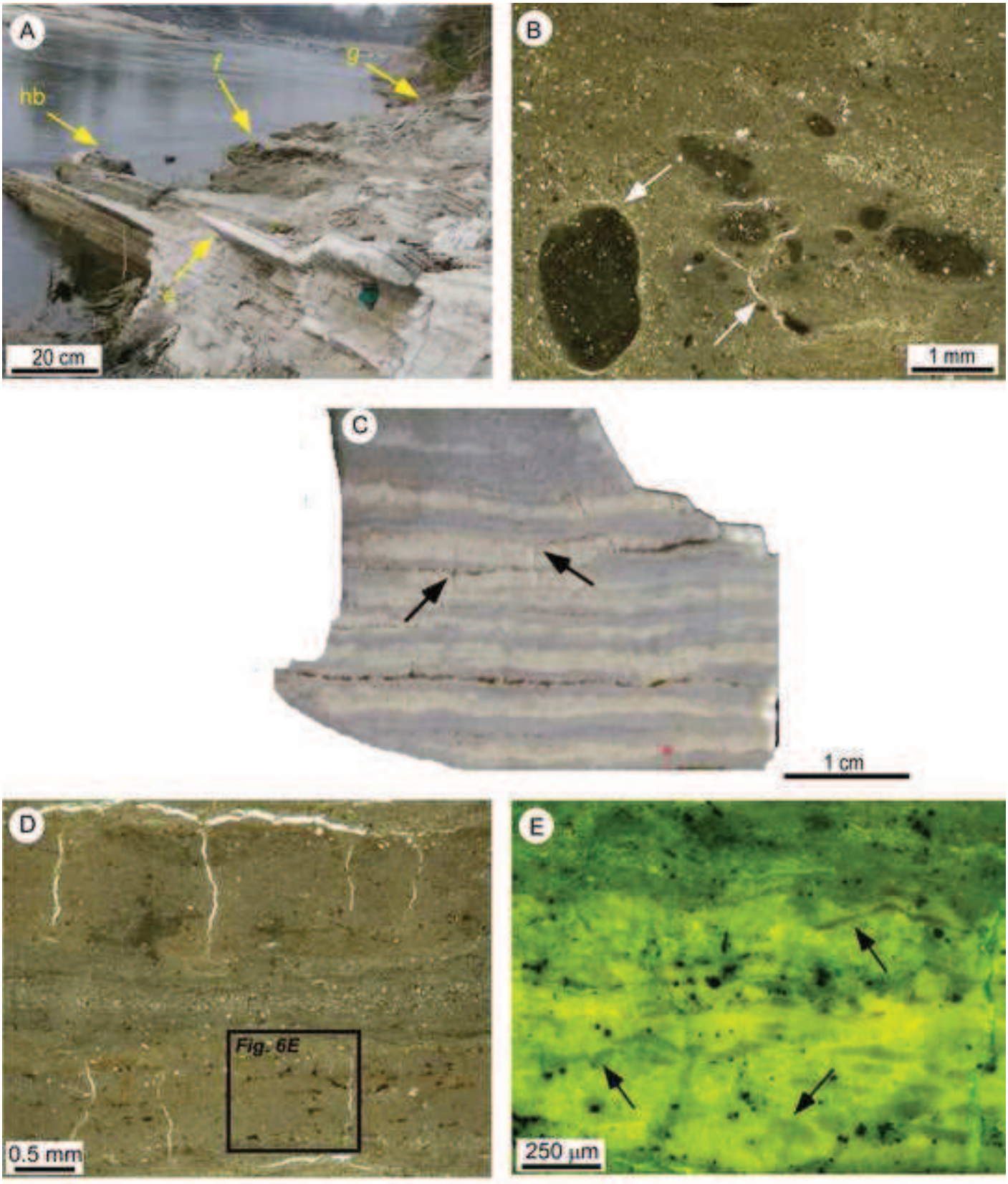

Dela Pierre et al. Fig. 6

Figure

Click here to download high resolution image

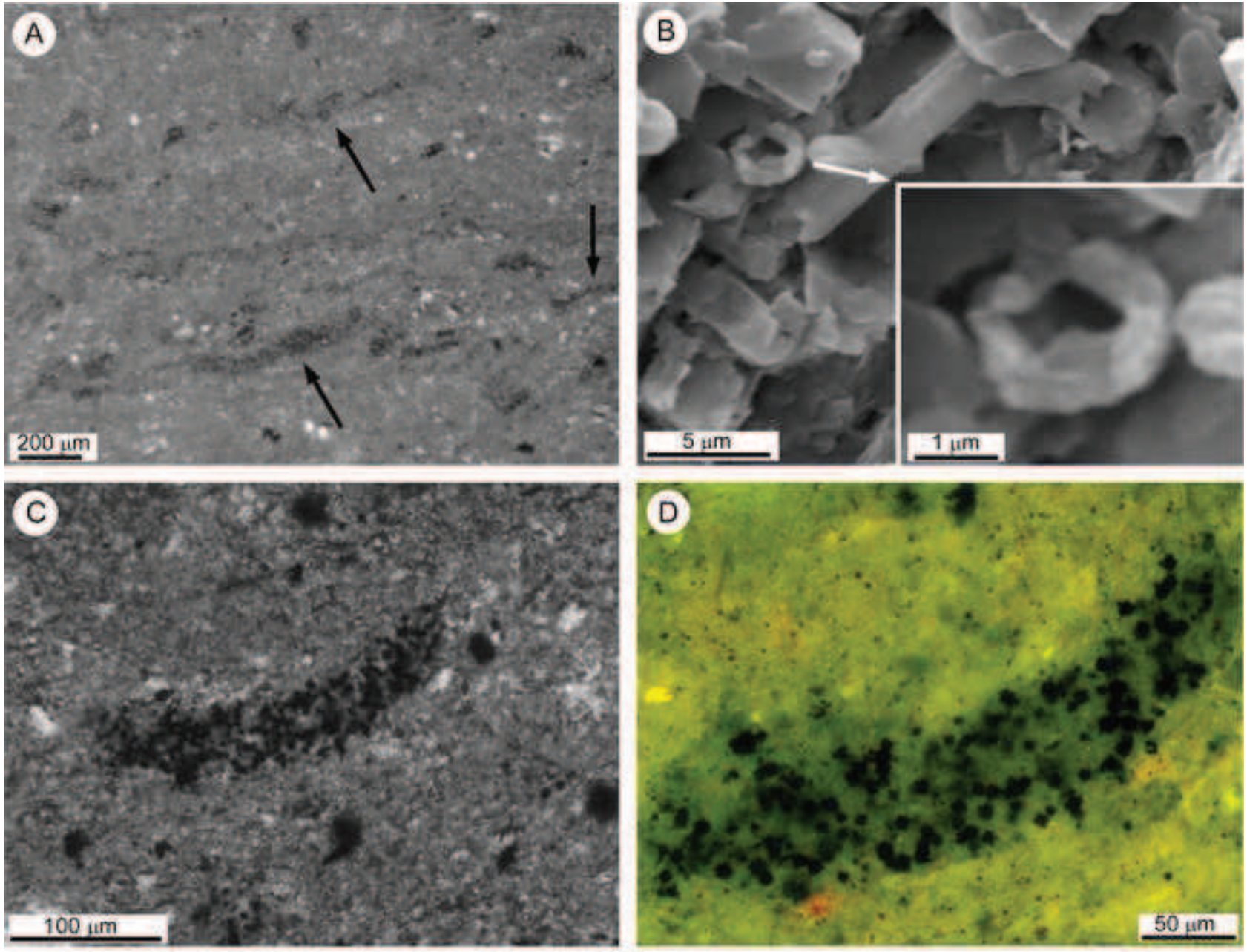

Dela Pierre et al. Fig. 7

Figure
Click here to download high resolution image

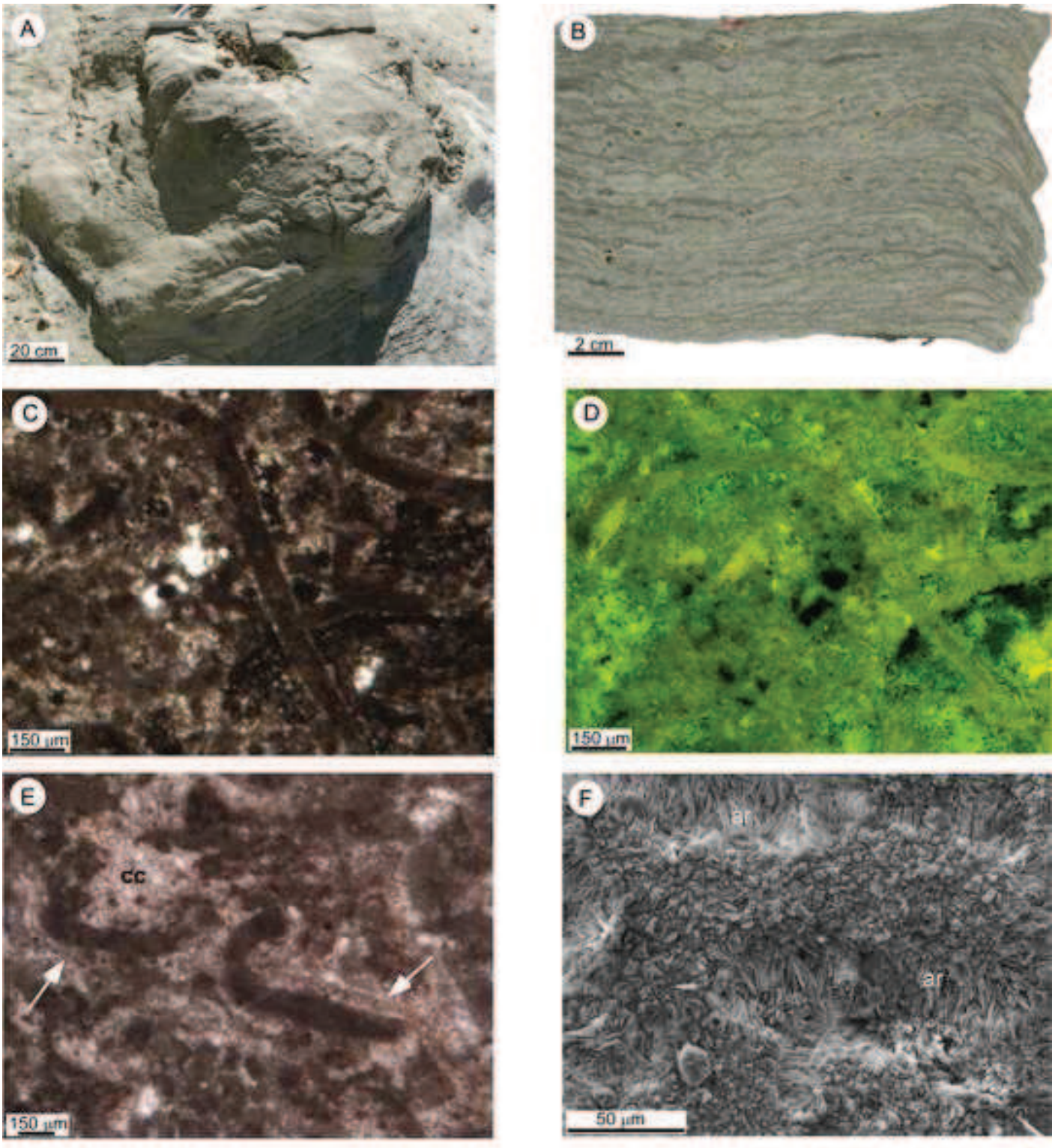

Dela Pierre et al. Fig. 8

Figure
Click here to download high resolution image

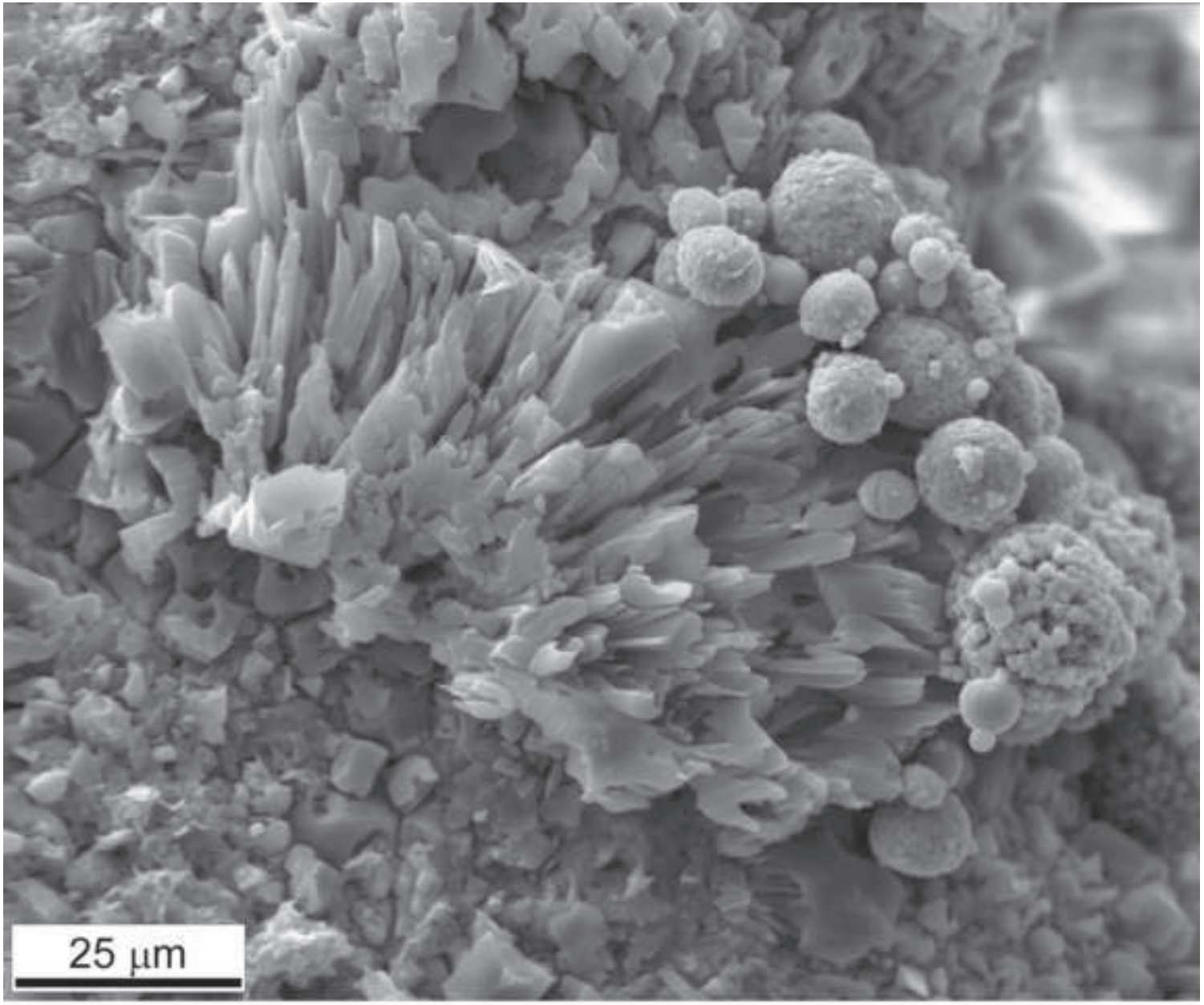

Dela Pierre et al. Fig. 9

Figure
Click here to download high resolution image

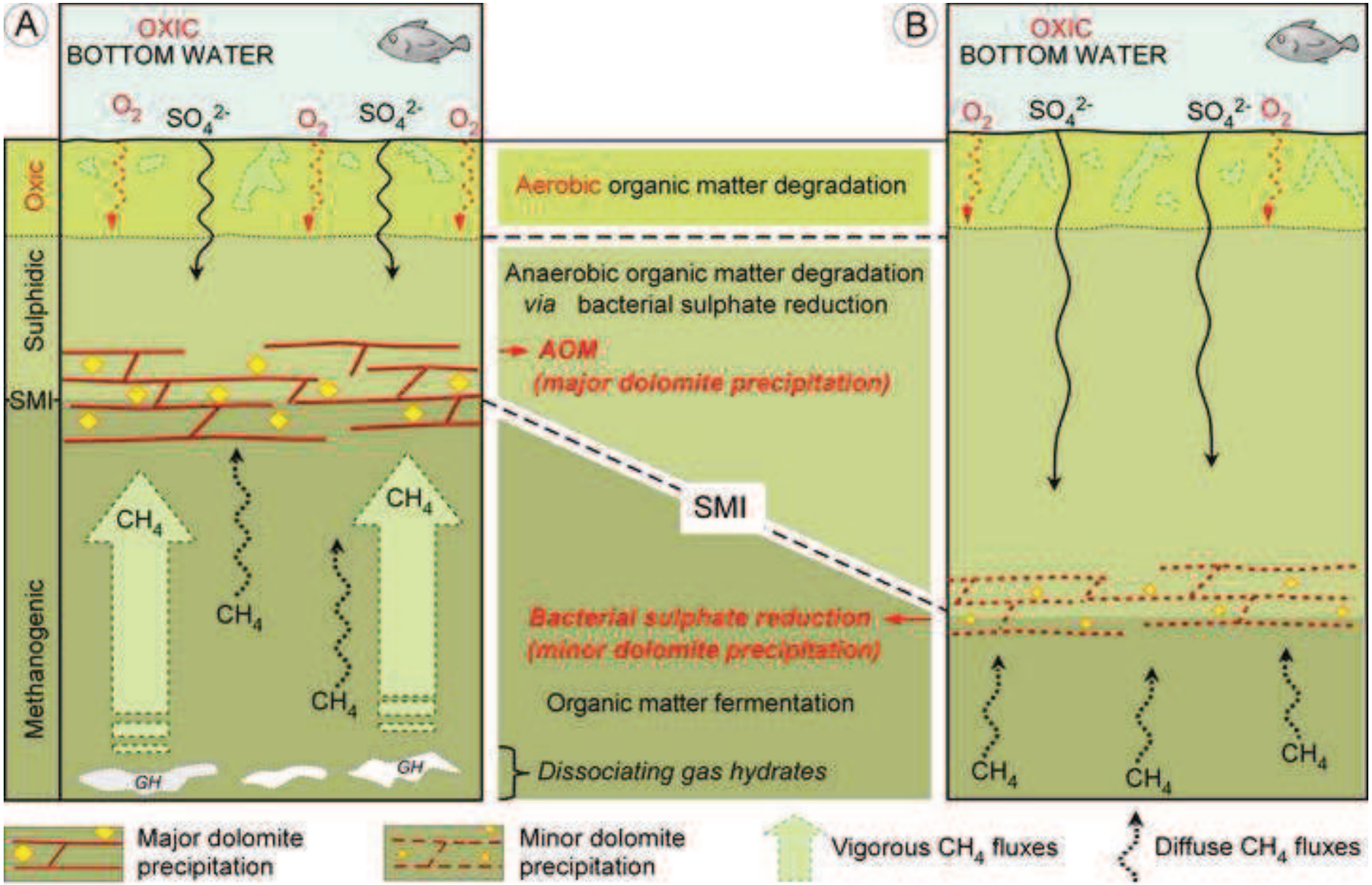

Dela Pierre et al., Fig. 10

Figure
Click here to download high resolution image

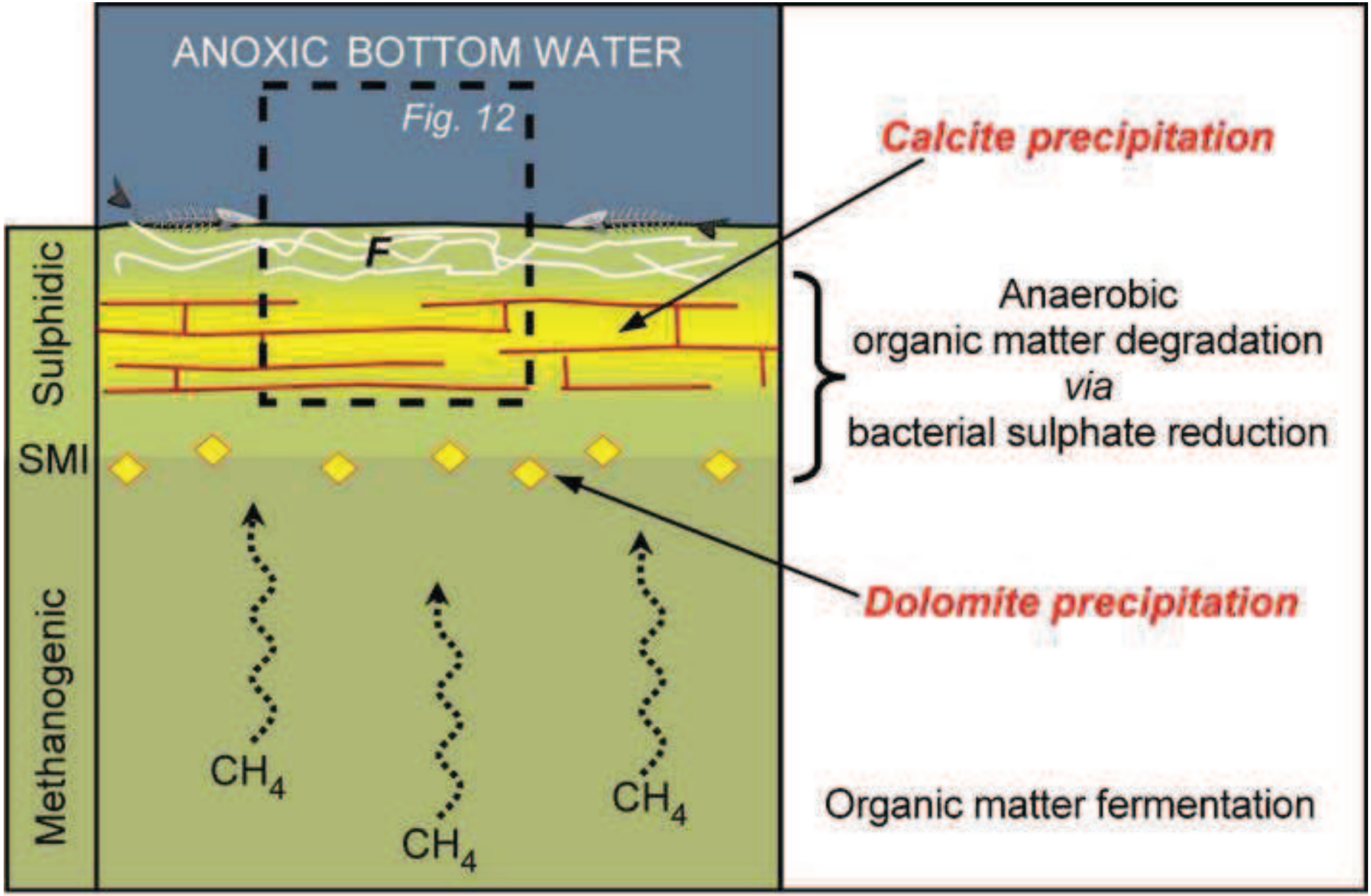

Dela Pierre et al., Fig. 11

Figure
Click here to download high resolution image

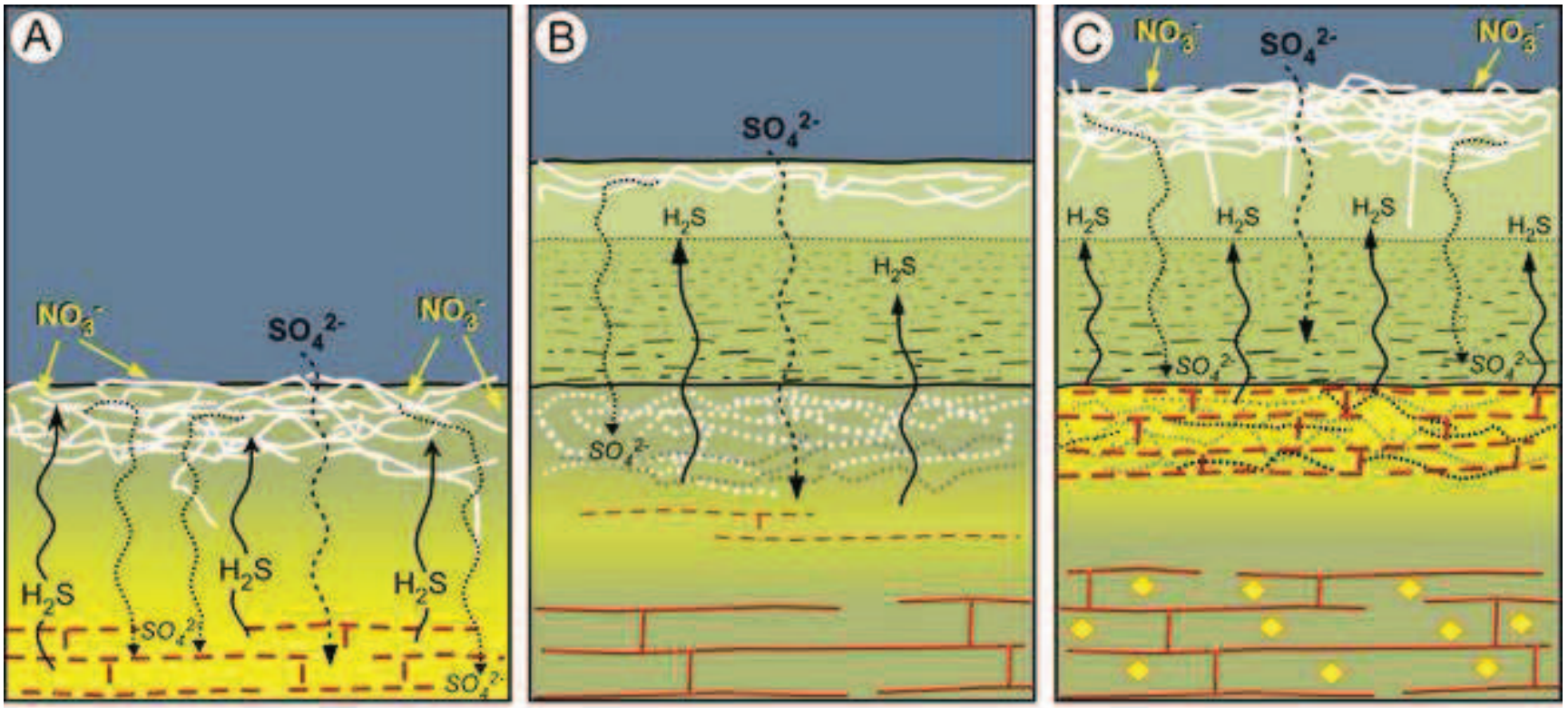

Dela Pierre et al., Fig. 12

Table
Click here to download Table: tab1.doc

Sample		*Cycle*	*T.C. [% on the whole rock]*	*Dolomite [% on the whole rock]*	*Calcite [% on the whole rock]*
PL7.1	(h.m.)	Pm7	40.7	39.4	1.3
FF7	**(bed g)**	**Pm7**	**59.0**	**3.1**	**55.9**
PL6.5	(l.s.)	Pm7	17.2	9.1	8.0
PL6.4	(l.s.)	Pm7	16.7	5.8	10.9
PL6.3	(l.s.)	Pm7	16.7	6.1	10.6
PL6.2	(l.s.)	Pm7	16.4	4.3	12.2
PL6.1	(l.s.)	Pm7	13.2	5.8	7.4
FF6	**(bed f)**	**Pm6**	**69.1**	**11.0**	**58.1**
PL 5.4	(l.s.)	Pm6	13.6	12.8	0.7
PL 5.3	(l.s.)	Pm6	23.4	20.1	3.3
PL 5.2	(l.s.)	Pm6	24.9	14.1	10.8
PL 5.1	(l.s.)	Pm5	30.7	25.4	5.2
FF5	**(bed e)**	**Pm5**	**84.6**	**16.7**	**67.9**
PL 4.6	(h.m.)	Pm5	30.3	27.1	3.2
PL 4.5	(l.s.)	Pm5	22.4	19.4	3.0
PL 4.4	(l.s.)	Pm5	16.1	13.3	2.8
PL 4.3	(l.s.)	Pm5	17.0	15.5	1.5
PL 4.2	(h.m.)	Pm4	39.1	18.3	20.8
PL 4.1	(h.m.)	Pm4	33.9	29.7	4.2
FF4	**(bed d)**	**Pm4**	**45.1**	**37.5**	**7.6**
PL3.5	(h.m.)	Pm4	31.6	12.3	19.3
PL3.4	(l.s.)	Pm4	17.2	5.1	12.1
PL3.3	(l.s.)	Pm4	20.4	4.2	16.3
PL3.2	(h.m.)	Pm3	15.7	5.0	10.7
PL3.1	**(bed c)**	**Pm3**	**48.2**	**24.9**	**23.3**
DOL3	**(bed c)**	**Pm3**	**36.1**	**20.3**	**15.9**
PL2.5	(h.m.)	Pm3	18.2	7.0	11.2
PL2.4	(l.s.)	Pm3	17.5	4.8	12.8
PL2.3	(h.m.)	Pm2	22.4	8.3	14.1
PL2.1	(h.m.)	Pm2	17.9	12.2	5.7
FF2	**(bed b)**	**Pm2**	**63.1**	**42.9**	**20.2**
PL1.6	(h.m.)	Pm2	23.0	20.5	2.5
PL1.5	(l.s.)	Pm2	9.7	2.6	7.2
PL1.4	(h.m.)	Pm2	15.1	11.7	3.5
PL1.3	(h.m.)	Pm1	29.6	12.1	17.5
PL1.2	(h.m.)	Pm1	23.5	10.4	13.1
DOL1	**(bed a)**	**Pm1**	**76.1**	**69.9**	**6.2**

Dela Pierre et al. Tab. 1

Table
Click here to download Table: tab2.doc

Sample		*Cycle*	*Dolomite* *[% vs T.C.]*	*Calcite* *[% vs T.C.]*
FF7	(bed g)	Pm7	5.2	94.8
FF6	(bed f)	Pm6	15.9	84.1
FF5	(bed e)	Pm5	19.8	80.2
FF4	(bed d)	Pm4	83.3	16.7
PL3.1	(bed c)	Pm3	51.7	48.3
DOL3	(bed c)	Pm3	56.0	44.0
FF2	(bed b)	Pm2	68.0	32.0
DOL1	(bed a)	Pm1	91.9	8.1

Dela Pierre et al., Tab. 2

Table

Click here to download Table: tab3.doc

Sample	*Cycle*	$\delta^{13}C_{cal}$ [‰]	$\delta^{18}O_{cal}$ [‰]	$\delta^{13}C_{dol}$ [‰]	$\delta^{18}O_{dol}$ [‰]
STR 8 (hem. body)	Pm6	–9.2	–7.2		
STR 7 (hem. body)	Pm6	–8.7	–6.9		
STR 4 (hem. body)	Pm6	–8.2	–7.7		
FF 7 (bed g)	**Pm7**	**–7.9**	**–8.8**	**–4.0**	**–5.8**
PL 6.4	Pm7	+0.5	–5.4		
PL 6.2	Pm7	–4.7	–6.4		
FF 6 (bed f)	**Pm6**	**–6.8**	**–7.9**	**–3.9**	**–6.1**
STR 8 (hem. body)	Pm6	–9.2	–7.2		
STR 7 (hem. body)	Pm6	–8.7	–6.9		
STR 4 (hem. body)	Pm6	–8.2	–7.7		
PL 5.4	Pm6	–0.4	–5.2		
PL 5.2	Pm6	–5.0	–6.0		
FF 5 (bed e)	**Pm5**	**–6.7**	**–6.5**	**–5.0**	**–4.9**
PL 4.4	Pm5	+0.3	–3.4		
PL 4.3	Pm5	0.0	–4.1		
FF 4 (bed d)	**Pm4**	**–5.7**	**–1.2**	**–5.2**	**+3.6**
PL 3.4	Pm4	+0.5	–5.1		
PL 3.2	Pm3	0.0	–3.3		
FF 3 (bed c)	**Pm3**	**–9.2**	**–3.9**	**–4.4**	**+1.3**
PL 2.4	Pm3	–1.0	–3.2		
FF 2 (bed b)	**Pm2**	**–14.5**	**–1.0**	**–21.0**	**+6.9**
PL 1.5	Pm2	–0.6	–5.1		
PL 1 .2	Pm1	–6.5	–2.5		
FF 1 (bed a)	**Pm1**	**-16.7**	**+5.7**	**–19.8**	**+7.0**

Dela Pierre et al., Tab. 3